

# QCD Corrections to Inelastic $J/\psi$ Photoproduction

MICHAEL KRÄMER \*

Deutsches Elektronen-Synchrotron DESY  
D-22603 Hamburg, Germany.

## Abstract

We present a complete calculation of the higher-order perturbative QCD corrections to inelastic photoproduction of  $J/\psi$  particles. A comprehensive analysis of total cross sections and differential distributions for the energy range of the fixed-target experiments and for inelastic  $J/\psi$  photoproduction at HERA is performed. The cross section and the  $J/\psi$  energy spectrum are compared with the available photoproduction data including first results from HERA. This analysis will not only provide information on the gluon distribution of the proton but appears to be a clean test for the underlying picture of quarkonium production as developed so far in the perturbative QCD sector.

# 1 Introduction

The measurement of the gluon distribution in the nucleon is one of the important goals of lepton-nucleon scattering experiments. The classical methods exploit the evolution of the nucleon structure functions with the momentum transfer and the size of the longitudinal structure function. With rising energies, however, jet physics and the production of heavy quark states become important complementary tools. Heavy flavour production in lepton-nucleon scattering is dominated by photon-gluon fusion and can thus yield direct information on the gluon distribution in the nucleon  $G(x, Q^2)$ . Besides open charm and bottom production, the formation of  $J/\psi$  bound states in inelastic photoproduction experiments

$$\gamma + \mathcal{N} \rightarrow J/\psi + X \tag{1}$$

provides an experimentally attractive method since  $J/\psi$  particles are easy to tag in the leptonic decay modes.

The production of heavy quarks in high energy photon-proton collisions can be calculated in perturbative QCD. The mass of the heavy quark,  $m_Q \gg \Lambda_{\text{QCD}}$ , acts as a cutoff and sets the scale for the perturbative calculations [1]. However, the subsequent transition from the colour-octet  $Q\bar{Q}$  pair to a physical quarkonium state introduces non-perturbative aspects. Two different mechanisms of bound state formation have been employed in previous analyses (for a recent review see Ref.[2]):

(i) The *local duality approach* [3] assumes that the colour-octet  $Q\bar{Q}$  pair rearranges itself into a colour-singlet bound state by the emission of non-perturbative soft gluons. According to the arguments of semi-local duality, one averages over all possible quarkonia states by integrating the perturbative cross section for inclusive  $Q\bar{Q}$  production from the quark threshold ( $= 2m_Q$ ) to the physical threshold for the production of a pair of heavy-light mesons ( $= 2m_D$  for the  $c\bar{c}$  system). The probability to generate a particular state, e.g.  $J/\psi$ , depends on different dynamical details of the production mechanism and cannot be absolutely predicted in this model. Another serious drawback of the duality approach is the fact that higher-order QCD corrections cannot be included since there is no unique way to decide what part of the radiatively emitted gluons are to be considered as a part of the bound state. Although dual models might describe some qualitative features of quarkonium production, they do not allow for a quantitative prediction and will therefore not be discussed in the present context.

(ii) In the *colour-singlet(CS) mechanism* [4–6] the quarkonium state is described by a colour-singlet  $Q\bar{Q}$  pair with the appropriate spin, angular-momentum and charge conjugation quantum numbers. In the static approximation, in which the motion of the charm quarks in the bound state is neglected, the production cross section factorizes into a short distance matrix element which describes the production of a  $Q\bar{Q}$  pair within a region of size  $1/m_Q$ , and a long distance factor that contains all the nonperturbative dynamics of the bound state formation. The short distance cross section can be calculated as a perturbative expansion in powers of the strong coupling constant  $\alpha_s(m_Q)$ , evaluated at a scale set approximately by the heavy quark mass, while the long-distance factor is related to the leptonic width.

A rigorous framework for treating quarkonium production and decays has recently been developed in Ref.[7] (see also Ref.[8]). The so-called factorization scheme is based on the use of non-relativistic QCD (NRQCD) [9] to separate the short distance parts from the long-distance matrix elements. The factorization approach explicitly takes into account the complete structure

of the quarkonium Fock space. For the production of  $S$ -wave quarkonia, like  $J/\psi$ , the colour-octet matrix elements associated with higher Fock states like  $|Q\bar{Q}g\rangle$  are suppressed by a factor of  $v^4$  compared to the leading colour-singlet contributions,  $v$  being the average velocity of the heavy quark in the quarkonium rest frame.<sup>1</sup> The NRQCD description of  $S$ -wave quarkonia production or annihilation thus reduces to the colour-singlet model in the non-relativistic limit  $v \rightarrow 0$ . It has been shown in the rigorous analysis of Ref.[7] that the factorization assumption of the CS model is correct for any specific  $S$ -wave process in the non-relativistic limit to all orders in  $\alpha_s$ .

Colour-octet matrix elements can become important if their associated short distance coefficient is enhanced compared to the colour-singlet contribution. It has recently been demonstrated that large  $p_\perp$  charmonium production in hadronic collisions can be accounted for in a satisfactory way by including both fragmentation mechanisms as well as higher Fock state contributions [11,12]. For the colour-octet matrix elements associated with the higher Fock states no simple relation exists in general between decay and production matrix elements. The corresponding contributions thus involve unknown non-perturbative parameters which, in the analyses Refs.[11,12], have been fitted to the experimental data. Once they have been measured in some production process they can be used to predict cross sections for different energies and different beam types. It should however be kept in mind that the analyses carried out so far are leading-order analyses. They are therefore plagued by large scale dependences and have to rely on the assumption that the perturbative expansion of the short-distance coefficients is well behaved and that the higher-order corrections do not strongly depend on the specific production mechanism and the collision energy. Moreover, it has been argued recently that important higher-twist effects have to be included in the theoretical description of charmonium hadroproduction [13]. These effects can yet not be predicted from first principles.

Many channels contribute to the generation of  $J/\psi$  particles in photoproduction experiments [14], similarly to the case of hadroproduction. Theoretical interest so far has focussed on two mechanisms for  $J/\psi$  photo- and electroproduction, elastic/diffractive [15,16] and inelastic production through photon-gluon-fusion [4]. While one expects to shed light on the physical nature of the pomeron by the first mechanism, inelastic  $J/\psi$  production provides information on the distribution of gluons in the nucleon [17]. The two mechanisms can be separated by measuring the  $J/\psi$  energy spectrum, described by the scaling variable

$$z = p \cdot k_\psi / p \cdot k_\gamma \quad (2)$$

with  $p, k_{\psi,\gamma}$  being the momenta of the nucleon and  $J/\psi, \gamma$  particles, respectively. In the nucleon rest frame,  $z$  is the ratio of the  $J/\psi$  to the  $\gamma$  energy,  $z = E_\psi/E_\gamma$ . For elastic/diffractive events  $z$  is close to one; a clean sample of inelastic events can be obtained in the range  $z \lesssim 0.9$  [18]. Reducible background mechanisms, such as  $B\bar{B}$  production with subsequent decay into  $J/\psi$  particles or resolved photon processes might become sizable at HERA energies but can be easily eliminated by applying suitable cuts [14].

In contrast to the case of hadroproduction, higher Fock state contributions to inelastic  $J/\psi$  photoproduction are strongly suppressed compared to the leading colour-singlet mechanism. Colour-octet contributions can become important only in the elastic domain,  $z \approx 1$ , where the short distance coefficient of the colour-singlet amplitude is suppressed by a factor  $\alpha_s$ . In the inelastic

---

<sup>1</sup>In the case of  $P$ -wave quarkonia, colour-singlet and colour-octet mechanisms contribute at the same order in  $v$  to annihilation rates and production cross sections and must therefore both be included for a consistent calculation [10].

region,  $z \lesssim 0.9$ , a perturbative gluon has to be emitted in the final state for kinematical reasons. This gluon carries off colour charge so that a colour-singlet state can be produced without any additional short-distance suppression. Since the non-perturbative matrix element associated with the colour-singlet state is enhanced compared to the colour-octet matrix element by a factor  $1/v^4$ , higher Fock state contributions to inelastic  $J/\psi$  photoproduction can safely be neglected. Fragmentation mechanisms dominate the production of  $J/\psi$  particles at large  $p_\perp$  [19] but their contribution to the total cross section is very small. As a result, the dominant mechanism for inelastic  $J/\psi$  photoproduction is by the colour-singlet state (as assumed in the CS model) and the cross section can be predicted without including unknown non-perturbative parameters.

A comparison of the leading-order predictions with photoproduction data of fixed-target experiments [20,21] reveals that the  $J/\psi$  energy dependence  $d\sigma/dz$  is adequately accounted for in the inelastic region  $z \lesssim 0.9$ . The theoretical calculation however underestimates the normalization of the measured cross section in general by more than a factor two, depending in detail on the  $J/\psi$  energy and the choice of the parameters [14]. The discrepancy with cross sections extrapolated from electroproduction data [22,23] is even larger.

The lowest-order approach to inelastic  $J/\psi$  photoproduction demands several theoretical refinements: (i) Relativistic corrections due to the motion of the charm quarks in the  $J/\psi$  bound state; (ii) Higher-order perturbative QCD corrections; and last but not least, (iii) Higher-twist effects which are not strongly suppressed due to the fairly low charm-quark mass. While the problem of higher-twist contributions has not been quantitatively approached so far (see Ref.[24] for a recent discussion), the relativistic corrections have been demonstrated to be under control in the inelastic region [25,26]. Including higher-order QCD corrections is, however, expected to be essential. Their contribution in general not only changes the overall normalization of the cross section but can also affect the shape of inclusive differential distributions. Expected *a priori* and verified subsequently, the QCD corrections dominate the relativistic corrections in the inelastic region, being of the order of several  $\alpha_s(M_{J/\psi}^2) \sim 0.3$ . In the first step of a systematic expansion, they can therefore be determined in the static approach [7].

In this work we present the complete calculation of the higher-order perturbative QCD corrections to inelastic  $J/\psi$  photoproduction; first results have already been published in Refs.[27–29]. We perform a comprehensive analysis of total cross sections and differential distributions for the energy range of the fixed-target experiments and for inelastic  $J/\psi$  photoproduction at HERA. A comparison of the next-to-leading order prediction with the experimental data will not only provide information on the gluon distribution of the proton but appears to be a clean test for the underlying picture of quarkonium production as developed in the perturbative QCD sector.

## 2 The Born cross section

Inelastic  $J/\psi$  photoproduction through photon-gluon fusion is described in leading order by the subprocess

$$\gamma(k_1) + g(k_2) \rightarrow J/\psi(P) + g(k_3) \quad (3)$$

as shown in Fig.1. Colour conservation and the Landau-Yang theorem [30] require the emission of a gluon in the final state. The cross section is generally calculated in the static approximation in which the motion of the charm quarks in the bound state is neglected. In this approximation the production amplitude factorizes into the short distance amplitude  $\mathcal{M}(\gamma + g \rightarrow c\bar{c} + g)$ , with  $c\bar{c}$  in

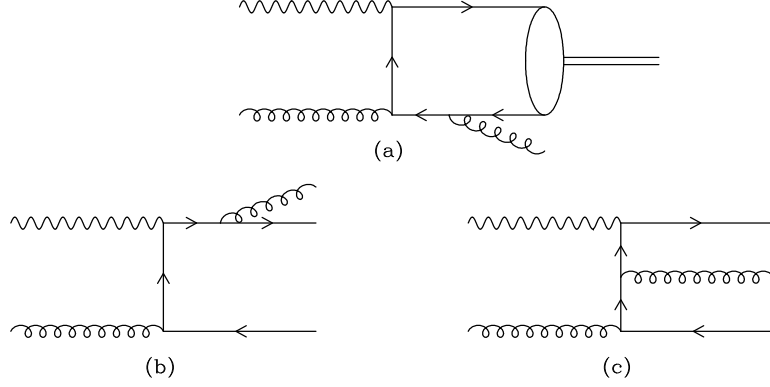


Figure 1: The leading-order Feynman diagrams contributing to inelastic  $J/\psi$  photoproduction. Additional graphs are obtained by reversing the arrows on the heavy quark lines.

the colour-singlet state and zero relative velocity of the quarks, and the wave function  $\varphi(0)$  of the  $J/\psi$  bound state at the origin:

$$\mathcal{M}(\gamma + g \rightarrow J/\psi + g) = \sqrt{\frac{2}{M_{J/\psi}}} \varphi(0) \text{Tr}\left\{\Pi_{S=1,s_z}(P_{J/\psi}, M_{J/\psi}) \mathcal{M}(\gamma + g \rightarrow c\bar{c} + g)\right\} \quad (4)$$

The spin projection operator  $\Pi$  combines the quark and antiquark spins to the appropriate triplet states. For negligible binding energy or, equivalently, for  $m_c = M_{J/\psi}/2$  one obtains [31]

$$\Pi_{S=1,s_z}(P_{J/\psi}, M_{J/\psi}) = \frac{1}{\sqrt{2}} \not{\varepsilon}(s_z) \frac{\not{P}_{J/\psi} + M_{J/\psi}}{2} \quad , \quad (5)$$

where  $\varepsilon^\mu(s_z)$  is the  $J/\psi$  polarization vector. The coupling strength of the  $J/\psi$  to the  $c\bar{c}$ -pair is specified in terms of the orbital wave function at the origin in momentum space. In leading order, the wave function is related to the leptonic width according to

$$\Gamma_{ee} = \frac{16\pi\alpha^2 e_c^2}{M_{J/\psi}^2} |\varphi(0)|^2 \quad . \quad (6)$$

We will describe the cross section in terms of the kinematical (pseudo-) Mandelstam variables

$$\begin{aligned} s_1 &\equiv s - M_{J/\psi}^2 = (k_1 + k_2)^2 - M_{J/\psi}^2 \\ t_1 &\equiv t - M_{J/\psi}^2 = (k_1 - P)^2 - M_{J/\psi}^2 \\ u_1 &\equiv u - M_{J/\psi}^2 = (k_2 - P)^2 - M_{J/\psi}^2 \end{aligned} \quad (7)$$

where  $s + t + u = M_{J/\psi}^2$ . All incoming and outgoing particles are taken to be on-mass-shell,  $k_1^2 = k_2^2 = k_3^2 = 0$  and  $P^2 = M_{J/\psi}^2$ . In the static approximation each of the heavy quarks carries one half the mass and one half the four-momentum of the  $J/\psi$ :

$$p_c = p_{\bar{c}} = P/2 \equiv p; \quad m_c = M_{J/\psi}/2; \quad \text{and} \quad p^2 = m_c^2 \equiv m^2 \quad . \quad (8)$$

From (4) we find for the amplitude of Fig.1(a)

$$\begin{aligned} \mathcal{M} &= \sqrt{\frac{2}{M_{J/\psi}}} \varphi(0) \frac{1}{2\sqrt{3}} \delta_{ab} g^2 e e_c \varepsilon^\mu(k_1) \varepsilon^\nu(k_2) \varepsilon^\lambda(k_3) \\ &\quad \times \frac{4}{\sqrt{2}} \text{Tr} \left\{ \not{\varepsilon}_{J/\psi}(s_z) (\not{p} + m) \gamma_\mu \frac{\not{p} - \not{k}_1 + m}{t_1} \gamma_\nu \frac{-\not{p} - \not{k}_3 + m}{s_1} \gamma_\lambda \right\} \quad . \end{aligned} \quad (9)$$

Here  $g$  and  $e$  are the strong and electromagnetic couplings respectively,  $g = \sqrt{4\pi\alpha_s}$ ,  $e = \sqrt{4\pi\alpha}$ , and  $e_c$  is the magnitude of the charm quark charge in units of  $e$ . Charge conjugation invariance implies that the Feynman graphs are symmetric under reversion of the fermion flow. All six amplitudes contributing to the leading-order cross section are proportional to the same colour factor  $1/\sqrt{3} \delta_{ij}$  ( $T^a T^b$ ) $_{ij} = 1/(2\sqrt{3}) \delta_{ab}$ , where  $a$  and  $b$  are the colour indices of the gluonic quanta. Gauge invariance ensures that we may sum over the spins of the initial photon and over the gluon spins by employing the substitutions  $\sum \varepsilon_\mu \varepsilon_\nu = -g_{\mu\nu}$ . To sum over the  $J/\psi$  spin states, we use  $\sum \varepsilon_{J/\psi}^\rho \varepsilon_{J/\psi}^\sigma = -g^{\rho\sigma} + P^\rho P^\sigma / M_{J/\psi}^2$ . Averaging over the initial photon/gluon helicities and colour the result for the cross section of the subprocess (3) may be written as [4]

$$\frac{d\sigma^{(0)}}{dt_1} = \frac{128\pi^2}{3} \frac{\alpha\alpha_s^2 e_c^2}{s^2} M_{J/\psi}^2 \frac{|\varphi(0)|^2}{M_{J/\psi}} \frac{s^2 s_1^2 + t^2 t_1^2 + u^2 u_1^2}{s_1^2 t_1^2 u_1^2} . \quad (10)$$

Although the cross section (10) is infrared finite it is not clear *a priori* in which kinematical region perturbative QCD can reliably be applied to  $J/\psi$  photoproduction. Indeed, at large  $z$  the  $J/\psi$  scatters more and more elastically and multiple soft gluon emission has to be considered. Similar effects might become important in the region where the transverse momentum  $p_\perp$  of the  $J/\psi$  tends towards zero. As discussed before, it is mandatory to require  $z \lesssim 0.9$  in order to eliminate contributions from elastic/diffractive production mechanisms. In Ref.[17] it has been argued that an additional cut on the transverse momentum of the  $J/\psi$ ,  $p_\perp \gtrsim 1$  GeV, has to be applied to define the truly inelastic region. This conclusion was, however, based on a comparison of leading-order cross sections with experimental data that have later been found to be contaminated from coherent production in the small  $p_\perp$  domain [22]. Accordingly, the region of applicability of perturbative QCD had not been clarified completely so far. As will become clear in Sec.5, the analysis of the next-to-leading order corrections restricts the kinematical domain where fixed-order calculations give a reliable description of inelastic  $J/\psi$  photoproduction. We will observe that the perturbative QCD calculation is not under proper control in the singular boundary region  $z \rightarrow 1$  and  $p_\perp \rightarrow 0$ , thereby indicating where multiple soft gluon emission becomes important.

### 3 The NLO cross section

Including higher-order QCD corrections to the partonic reaction (3) is expected to be essential for the theoretical description of inelastic  $J/\psi$  photoproduction. Next-to-leading order corrections to open heavy flavour photoproduction have been calculated over the recent years [32,33]. They have been found to increase the normalization of the cross section significantly without strongly affecting the shape of the inclusive differential distributions. These results can however not directly be transferred to the case of bound state production as will become clear in Sec.5. It is thus important to investigate how the features of the lowest-order  $J/\psi$  photoproduction cross section are modified by radiative corrections and by including new production mechanisms which contribute in next-to-leading order.

In this work we present a complete calculation of the higher-order perturbative QCD corrections to inelastic  $J/\psi$  photoproduction. Results for total cross sections and the  $J/\psi$  energy and transverse momentum spectrum will be discussed. The photon-parton reactions which contribute to the

inclusive cross sections up to order  $\alpha\alpha_s^3$  are

$$\begin{aligned}
\gamma + g &\rightarrow (Q\bar{Q}) + g && \mathcal{O}(\alpha\alpha_s^2), \mathcal{O}(\alpha\alpha_s^3) \\
\gamma + g &\rightarrow (Q\bar{Q}) + g + g && \mathcal{O}(\alpha\alpha_s^3) \\
\gamma + g &\rightarrow (Q\bar{Q}) + q + \bar{q} && \mathcal{O}(\alpha\alpha_s^3) \\
\gamma + q(\bar{q}) &\rightarrow (Q\bar{Q}) + g + q(\bar{q}) && \mathcal{O}(\alpha\alpha_s^3)
\end{aligned}$$

including virtual corrections to the leading-order process. We choose a renormalization and factorization scheme in which the massive particles are decoupled smoothly for momenta smaller than the heavy quark mass [34]. This implies that the heavy quark does not contribute to the evolution of the QCD coupling and of the structure functions. Furthermore, there are no contributing subprocesses initiated by an intrinsic heavy flavour coming directly from the structure function of the proton. All effects of the heavy quark are contained in the parton cross section.

The calculation of the the next-to-leading order corrections will be outlined in this section. More details can be found in the Appendices.

### 3.1 Virtual corrections

The evaluation of the  $\mathcal{O}(\alpha_s)$  corrections to inelastic  $J/\psi$  photoproduction involves the calculation of the virtual cross section obtained from the interference term between the virtual and the Born amplitude. For the unrenormalized virtual cross section one finds in  $n \equiv 4 - 2\epsilon$  dimensions

$$\begin{aligned}
\left[ s^2 \frac{d^2\sigma^{(1)}}{dt_1 du_1} \right]^V &= \frac{1}{(N^2 - 1)} \frac{1}{4(1 - \epsilon)^2} \frac{\pi(4\pi)^{-2+\epsilon}}{\Gamma(1 - \epsilon)} \left( \frac{t_1 u_1 - 4m^2 s}{\mu^2 s} \right)^{-\epsilon} \\
&\quad \times \delta(s_1 + t_1 + u_1 + 8m^2) \sum 2 \operatorname{Re}(\mathcal{M}^B \mathcal{M}^{V*}) \quad , \quad (11)
\end{aligned}$$

where  $1/(N^2 - 1)$  is the colour average factor for the gluon in the initial state and  $N$  denotes the number of colours. Photons and gluons have  $n - 2$  spin degrees of freedom resulting in the spin average factor  $1/(n - 2)^2 = 1/4(1 - \epsilon)^2$ . The parameter  $\mu$  has the dimensions of a mass and is introduced in order to compensate for the dimensionality of the gauge coupling constants in  $n$  dimensions.

The Feynman gauge has been adopted to evaluate the 105 diagrams which contribute to the virtual amplitude. Charge conjugation invariance implies that the graphs are symmetric under reversion of the fermion flow. The ultraviolet (UV), infrared (IR), and the collinear or mass (M) singularities have been treated by using  $n$  dimensional regularization and show up as single and double pole terms of the type  $\epsilon^{-i}$  ( $i = 1, 2$ ). We have refrained from adopting the seemingly simpler scheme of dimensional reduction which however gives rise to complications in the massive quark case as pointed out in Ref.[35]. The Feynman integrals containing loop momenta in the numerator have been reduced to a set of scalar integrals using an adapted version of the reduction program outlined in Ref.[36]. This program has been extended to treat  $n$  dimensional tensor integrals with linear dependent propagators in order to account for the IR- and M-singularities and the special kinematical situation which is encountered in the nonrelativistic approximation to  $J/\psi$  photoproduction. The scalar integrals have been calculated by the Feynman parametrization technique and analytical results are listed in Appendix A.

The UV-divergences which are contained in the fermion self energy graphs and the vertex corrections shown in Fig.2, are removed by renormalization of the heavy quark mass and the

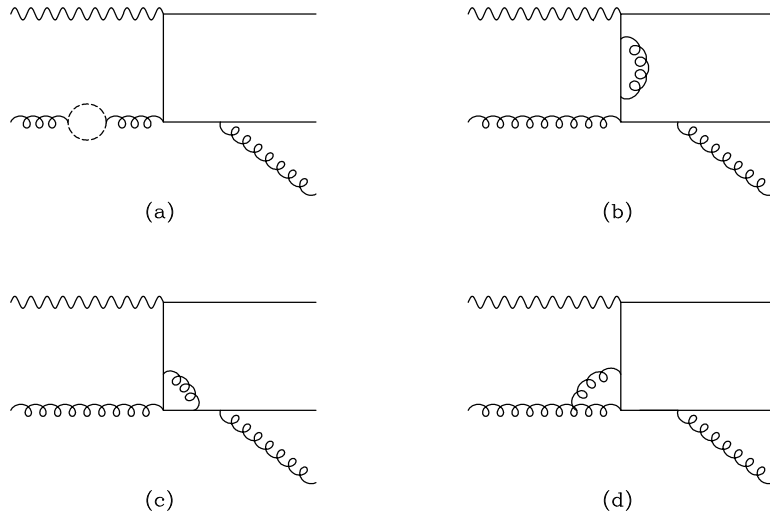


Figure 2: Generic Feynman diagrams contributing to the virtual amplitude (part 1): self-energy corrections (a,b) [36 diagrams], abelian vertex corrections ( $\gamma c\bar{c}$ - and  $g c\bar{c}$ -vertices) (c) [18 diagrams], and non-abelian vertex corrections (d) [12 diagrams].

QCD coupling. The masses of the light quarks appearing in the fermion loops in Fig.2a have been neglected while the mass parameter of the heavy quark has been defined in the on-mass-shell scheme. The renormalization of the QCD coupling has been carried out in the extended  $\overline{\text{MS}}$  scheme introduced in Ref.[34] and adopted in previous calculations of open heavy flavour production [37,32,33]. In this scheme the effects of heavy flavours are smoothly decoupled for momenta much smaller than the heavy quark mass. The bare coupling has to be replaced according to

$$\begin{aligned}
 g_{\text{bare}} &= Z_g g(\mu_R^2) \\
 &= g(\mu_R^2) \left[ 1 - \frac{\alpha_s(\mu_R^2)}{8\pi} \left\{ \left( \frac{1}{\epsilon} - \gamma_E + \ln 4\pi - \ln \left( \frac{\mu_R^2}{\mu^2} \right) \right) \beta_0 + \frac{2}{3} \ln \left( \frac{m^2}{\mu_R^2} \right) \right\} \right] \quad , \quad (12)
 \end{aligned}$$

with  $\beta_0 = (11N - 2n_f)/3$ . The total number of flavours including the heavy quark is denoted by  $n_f$  and  $n_{\text{lf}} = n_f - 1$  is the number of light quarks. The renormalization constant  $Z_g$  is defined such that the contribution of the heavy-fermion loop in the gluon self energy graphs is cancelled in the renormalized cross section for small momenta flowing into the heavy-fermion loop. The UV-divergences arising from gluon or light fermion loops are removed according to the standard  $\overline{\text{MS}}$  subtraction scheme [38]. For the renormalization scale evolution of the strong coupling one obtains from (12)

$$\frac{\partial g^2}{\partial \ln \mu_R^2} = g \beta(g) = -\alpha_s^2(\mu_R^2) \left( \beta_0 + \frac{2}{3} \right) = -\alpha_s^2(\mu_R^2) \beta_0(n_{\text{lf}}) \quad . \quad (13)$$

The extended  $\overline{\text{MS}}$  scheme thus implies that the heavy quark does not contribute to the evolution of the QCD coupling so that  $\alpha_s$  has to be evaluated using  $n_{\text{lf}}$  active flavours.

Besides the self-energy diagrams and vertex corrections, 39 box graphs contribute to the virtual amplitude, which can be grouped in eight classes as shown in Fig.3. All diagrams falling into one particular class are related by exchange of photon or gluon momenta, adjustment of the colour factor and reversion of the fermion flow. These relations have been checked explicitly.



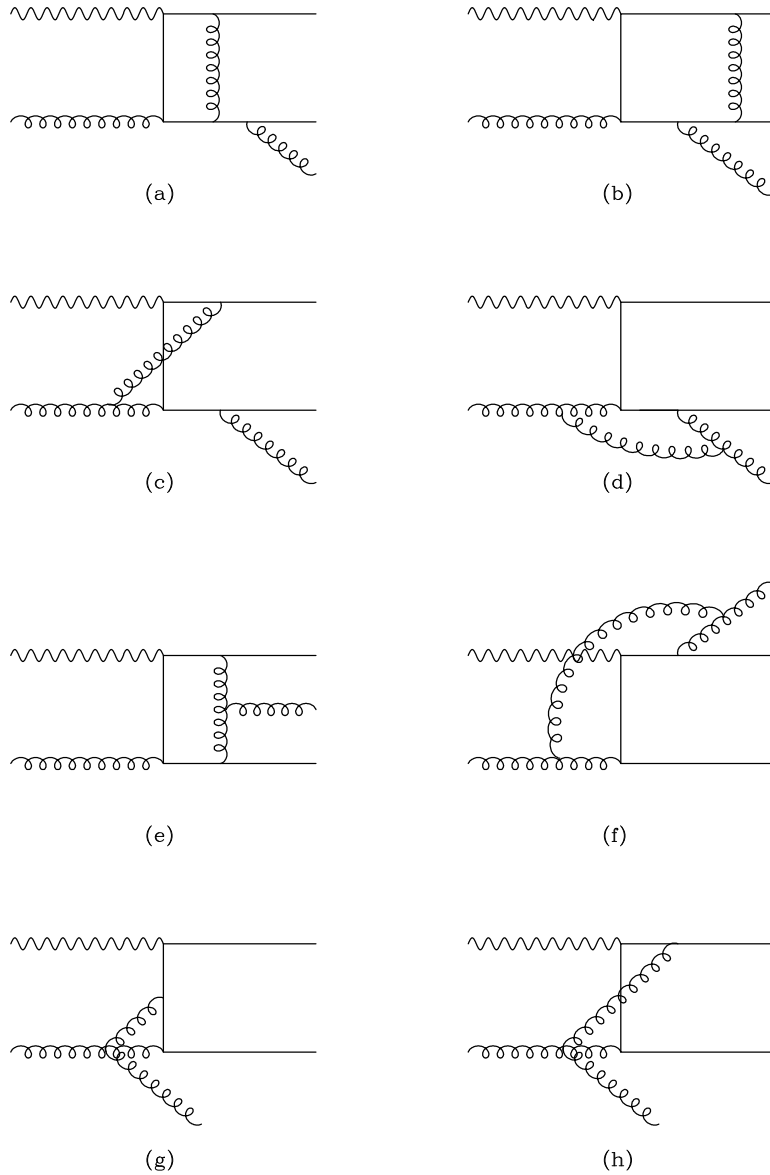


Figure 3: Generic Feynman diagrams contributing to the virtual amplitude (part 2): abelian four-point box graphs (a) [12 diagrams], abelian five-point box graphs (b) [6 diagrams], non-abelian four-point box graphs (c) [8 diagrams] and (d) [4 diagrams], non-abelian five-point box graphs (e) [4 diagrams] and (f) [2 diagrams], and diagrams involving four-gluon couplings (g) [2 diagrams] and (h) [1 diagram].

The exchange of longitudinal gluons between the massive quarks in diagram Fig.3b leads to the Coulombic singularity  $\sim \pi^2/v$  which can be isolated by introducing a small relative quark velocity  $v$  (see Appendix A for details). For the Coulomb-singular part of the virtual cross section we find

$$\sigma = |\varphi(0)|^2 \hat{\sigma}^{(0)} \left( 1 + \frac{\alpha_s}{\pi} C_F \frac{\pi^2}{v} + \frac{\alpha_s}{\pi} \hat{C} + \mathcal{O}(\alpha_s^2) \right) , \quad (14)$$

where the colour factor is given by  $C_F = (N^2 - 1)/(2N)$ . The final state interaction in the colour-singlet channel is attractive and has to be interpreted as the Sommerfeld rescattering correction [39] which can be associated with the inter-quark potential of the bound state. The Coulomb-singular part of the virtual cross section is universal appearing in the next-to-leading order corrections to all production and decay processes involving  $S$ -wave quarkonia. Following the standard path [40], the corresponding contribution has to be factored out and mapped into the  $c\bar{c}$  wave function:

$$\sigma = |\varphi(0)|^2 \left( 1 + \frac{\alpha_s}{\pi} C_F \frac{\pi^2}{v} \right) \hat{\sigma}^{(0)} \left[ 1 + \frac{\alpha_s}{\pi} \hat{C} + \mathcal{O}(\alpha_s^2) \right] \Rightarrow |\varphi(0)|^2 \hat{\sigma}^{(0)} \left[ 1 + \frac{\alpha_s}{\pi} \hat{C} + \mathcal{O}(\alpha_s^2) \right] . \quad (15)$$

Only the exchange of transversal gluons contributes to the next-to-leading order expressions for the hard parton cross section.

### 3.2 Real corrections

The evaluation of the  $\mathcal{O}(\alpha\alpha_s^3)$  cross section requires the calculation of the gluon bremsstrahlung reaction

$$\gamma(k_1) + g(k_2) \rightarrow J/\psi(2p) + g(k_3) + g(k_4) \quad (16)$$

and processes where the final-state gluon splits into light quark-antiquark pairs

$$\gamma(k_1) + g(k_2) \rightarrow J/\psi(2p) + q(k_3) + \bar{q}(k_4) . \quad (17)$$

The 48 Feynman diagrams which contribute to the amplitude can be obtained from the generic ones shown in Fig.4 by permutation of the photon and gluon lines. Spin and colour projection imply that the diagrams are invariant under reversion of the fermion flow. For the cross section of the two-gluon final states (16), averaged over initial spins and colours, one obtains (see Appendix B.1)

$$\left[ s^2 \frac{d^2\sigma^{(1)}}{dt_1 du_1} \right]^R = \frac{1}{2!} \frac{1}{(N^2 - 1)} \frac{1}{4(1 - \epsilon)^2} \frac{\mu^{2\epsilon} (4\pi)^{-4+2\epsilon}}{2\Gamma(1 - 2\epsilon)} \left( \frac{t_1 u_1 - 4m^2 s}{\mu^2 s} \right)^{-\epsilon} \times s_3^{-\epsilon} \int d\Omega_n \sum |\mathcal{M}^R|^2 , \quad (18)$$

where

$$\begin{aligned} s &= (k_1 + k_2)^2 \equiv s_1 + 4m^2 \\ t_1 &= (2p - k_1)^2 - 4m^2 \\ u_1 &= (2p - k_2)^2 - 4m^2 , \end{aligned} \quad (19)$$

$s_3 = (k_3 + k_4)^2 = s_1 + t_1 + u_1 + 8m^2$  and  $d\Omega_n = d\theta_1 \sin^{n-3} \theta_1 d\theta_2 \sin^{n-4} \theta_2$ . The angles  $\theta_1$  and  $\theta_2$  which describe the orientation of the outgoing light partons are defined in Appendix B.1. A factor  $1/2!$  has to be included since there are two identical particles in the final state. For the cross section of the light-quark-antiquark-splitting reaction (17) this factor has to be dropped.

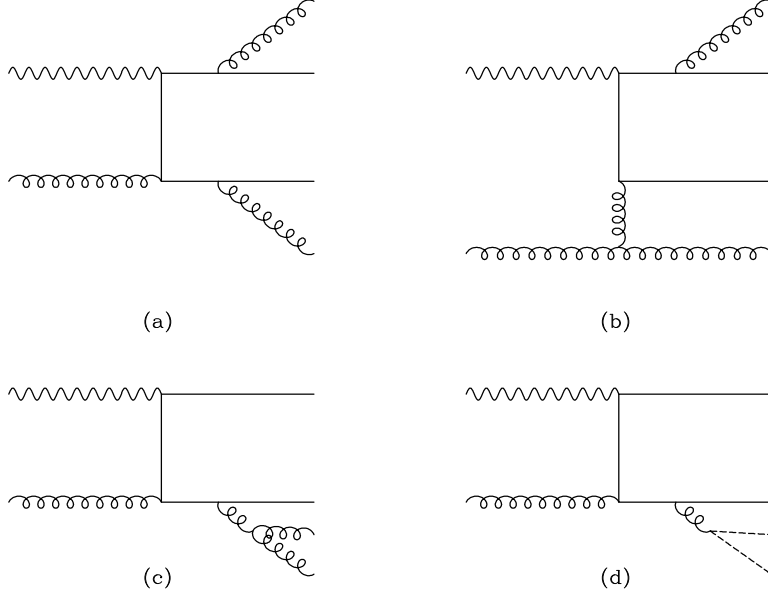


Figure 4: Generic Feynman diagrams contributing to the gluon bremsstrahlung process (a-c) and the quark-antiquark splitting reaction (d).

The real-gluon cross section contains IR and M singularities so that the square of the amplitude had to be calculated in  $n$  dimensions up to order  $\epsilon^2$ . For the sum of the gluon polarization we have used  $\sum \varepsilon_\mu \varepsilon_\nu = -g_{\mu\nu}$  and the unphysical longitudinal gluon polarizations have been removed by adding ghost contributions.

The computation of the real cross section has been performed by adopting the phase space slicing method as outlined in Ref.[41] and used in previous calculations of open heavy flavour production [35,33,42]. We have split the cross section into an infrared-collinear part ( $s_3 \leq \Delta$ ), which contains all singularities due to soft gluon emission and splitting of the final state gluon into gluon and light quark-antiquark pairs, and a hard-gluon part ( $s_3 > \Delta$ ). The cut-off parameter  $\Delta$  is chosen such that it can be neglected with respect to mass terms like  $m^2$  and the kinematical invariants  $s_1$ ,  $t_1$ , and  $u_1$ . In the final answer the limit  $\Delta \rightarrow 0$  is carried out. The hard-gluon part ( $s_3 > \Delta$ ) contains single pole terms which are associated with initial state gluon radiation only. These collinear divergences have to be absorbed into the renormalization of the parton densities as outlined in Sec.3.4. To perform the integration over the orientation of the final state gluons or light quarks the matrix element squared has been decomposed into sums of terms which have at most two factors containing the dependence on the polar angle  $\theta_1$  and the azimuthal angle  $\theta_2$ . This decomposition is described in Appendix B.1.

The infrared-collinear cross section ( $s_3 \leq \Delta$ ) for the two-gluon final states (16) is obtained from the expression

$$\begin{aligned}
 \left[ s^2 \frac{d\sigma^{(1)}}{dt_1 du_1} \right]^S &= \frac{1}{2!} \frac{1}{(N^2 - 1)} \frac{1}{4(1 - \epsilon)^2} \frac{\mu^{2\epsilon} (4\pi)^{-4+2\epsilon}}{2\Gamma(1 - 2\epsilon)} \left( \frac{t_1 u_1 - 4m^2 s}{\mu^2 s} \right)^{-\epsilon} \delta(s_1 + t_1 + u_1 + 8m^2) \\
 &\quad \times \int_0^\Delta ds_3 s_3^{-\epsilon} \int d\Omega_n \sum |\mathcal{M}^R|^2 \quad . \quad (20)
 \end{aligned}$$

For the light-quark-antiquark final state the symmetry factor  $1/2!$  has to be dropped. The calculation of the infrared-collinear cross section (20) is described in detail in Appendix B.2. Adding

the resulting expression (101,102) to the virtual correction leads to a cancellation of the infrared singularities.

### 3.3 The photon-quark subprocess

The cross section in next-to-leading order involves a new production mechanism where the photon is scattered off a light (anti-)quark from the proton

$$\gamma(k_1) + q(\bar{q})(k_2) \rightarrow J/\psi(2p) + g(k_3) + q(\bar{q})(k_4) \quad . \quad (21)$$

Because of spin and colour projection the  $J/\psi$  particle can only be produced in the Bethe-Heitler reaction shown in Fig.5. The amplitude of the  $\gamma q(\bar{q})$  subprocess does not depend on the electric charge of the light quarks. Averaging over spin and colour of the initial state particles the  $\gamma q(\bar{q})$

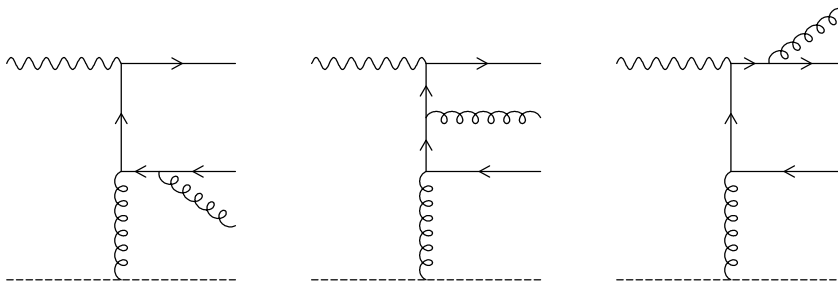


Figure 5: Feynman diagrams contributing to the photon-(anti)quark subprocess  $\gamma q(\bar{q}) \rightarrow J/\psi g q(\bar{q})$ . Additional graphs are obtained by reversing the arrows on the heavy quark lines.

cross section is given by

$$s^2 \frac{d^2 \sigma_{q\gamma}^{(1)}}{dt_1 du_1} = n_{\text{lf}} \frac{1}{N} \frac{1}{4(1-\epsilon)} \frac{\mu^{2\epsilon} (4\pi)^{-4+2\epsilon}}{2\Gamma(1-2\epsilon)} \left( \frac{t_1 u_1 - 4m^2 s}{\mu^2 s} \right)^{-\epsilon} s_3^{-\epsilon} \int d\Omega_n \sum |\mathcal{M}_{q\gamma}|^2 \quad . \quad (22)$$

The cross section (22) contains collinear divergences  $\sim 1/\epsilon$  due to gluon emission from the initial-state light (anti-)quark which have to be removed by mass factorization.

### 3.4 Mass factorization

The collinear singularities contained in the hard-gluon bremsstrahlung reaction and the  $\gamma q(\bar{q})$  subprocess are universal and can be absorbed, as usual, into the renormalization of the parton densities. According to the factorization theorem [1] the parton cross section can be written as

$$\frac{d^2 \sigma_{\gamma i}(s, t_1, u_1, \mu^2, \epsilon)}{dt_1 du_1} = \int_0^1 dx x \Gamma_{gi}(x, Q^2, \mu^2, \epsilon) \frac{d^2 \hat{\sigma}_{\gamma g}(\hat{s}, t_1, \hat{u}_1, Q^2)}{dt_1 d\hat{u}_1} \quad , \quad (23)$$

where  $\hat{s} = xs$ ,  $\hat{u}_1 = xu_1$  and  $i = g, q(\bar{q})$ . The reduced cross sections  $d\hat{\sigma}_{\gamma g}$  and  $d\hat{\sigma}_{\gamma q(\bar{q})}$  defined by the above equation are free of collinear singularities and depend on the mass factorization scale  $Q^2$ . This scale separates long and short distance effects and is a priori only determined to be of the order of the heavy quark mass  $m$ . The collinear singularities are contained in the splitting

functions  $\Gamma_{gi}$  of the incoming partons (gluons or light quarks). The splitting functions depend on the mass factorization scale  $Q^2$  and further on the parameter  $\mu^2$  which is an artefact of  $n$ -dimensional regularization. Up to leading order in  $\alpha_s$  they are given by [43]

$$\Gamma_{ij}(x, Q^2, \mu^2, \epsilon) = \delta_{ij} \delta(1-x) + \frac{\alpha_s}{2\pi} \left[ -\frac{1}{\epsilon} P_{ij}(x) + f_{ij}(x, Q^2, \mu^2) \right] , \quad (24)$$

where the universal Altarelli-Parisi splitting kernels [44] are denoted by  $P_{ij}(x)$ . The finite functions  $f_{ij}$  are completely arbitrary, different choices corresponding to different factorization schemes. Here we have adopted the  $\overline{\text{MS}}$ -scheme corresponding to

$$f_{ij}^{\overline{\text{MS}}}(x, Q^2, \mu^2) = P_{ij}(x) \left( \gamma_E - \ln 4\pi + \ln \frac{Q^2}{\mu^2} \right) . \quad (25)$$

For the reduced cross section of the  $\gamma$ -gluon process one finds from (23)

$$\begin{aligned} \frac{d^2 \hat{\sigma}_{\gamma g}^{(1)}(s, t_1, u_1, Q^2)}{dt_1 du_1} &= \frac{d^2 \sigma_{\gamma g}^{(1)}(s, t_1, u_1, \mu^2, \epsilon)}{dt_1 du_1} \\ &- \frac{\alpha_s}{2\pi} \int_0^1 dx x P_{gg}(x) \left[ -\frac{1}{\epsilon} + \gamma_E - \ln 4\pi + \ln \frac{Q^2}{\mu^2} \right] \frac{d^2 \sigma_{\gamma g}^{(0)}(xs, t_1, xu_1)}{dt_1 d\hat{u}_1} . \end{aligned} \quad (26)$$

The corresponding expression for the  $\gamma - q(\bar{q})$  scattering reaction reads

$$\begin{aligned} \frac{d^2 \hat{\sigma}_{\gamma q}^{(1)}(s, t_1, u_1, Q^2)}{dt_1 du_1} &= \frac{d^2 \sigma_{\gamma q}^{(1)}(s, t_1, u_1, \mu^2, \epsilon)}{dt_1 du_1} \\ &- \frac{\alpha_s}{2\pi} \int_0^1 dx x P_{gq}(x) \left[ -\frac{1}{\epsilon} + \gamma_E - \ln 4\pi + \ln \frac{Q^2}{\mu^2} \right] \frac{d^2 \sigma_{\gamma q}^{(0)}(xs, t_1, xu_1)}{dt_1 d\hat{u}_1} . \end{aligned} \quad (27)$$

The Altarelli-Parisi kernel  $P_{gg}(x)$  of the gluon-splitting function has the form

$$\begin{aligned} P_{gg}(x) &= N \left[ \Theta(1-x-\delta) \cdot 2 \left\{ \frac{1-x}{x} + \frac{x}{1-x} + x(1-x) \right\} \right. \\ &\quad \left. + \delta(1-x) \left( 2 \ln \delta + \frac{11}{6} \right) \right] - \frac{1}{3} n_{\text{lf}} \delta(1-x) , \end{aligned} \quad (28)$$

where the number of light flavours is denoted by  $n_{\text{lf}}$ . We have adopted the convention introduced in Ref.[41] to regulate the pole at  $x = 1$ . The parameter  $\delta$  allows one to distinguish between soft ( $x > 1 - \delta$ ) and hard ( $x < 1 - \delta$ ) gluons and is related to the cut-off parameter  $\Delta$  by  $\delta = \Delta/(s + u_1)$ . Finally, the Altarelli-Parisi kernel  $P_{gq}$  appearing in (27) is given by

$$P_{g\bar{q}}(x) = P_{gq}(x) = C_F \left[ \frac{1 + (1-x)^2}{x} \right] . \quad (29)$$

After mass factorization and cancellation of the infrared singularities between the virtual corrections and the contribution of soft gluon emission we obtain a finite expression for the  $\mathcal{O}(\alpha_s^3)$  inelastic  $J/\psi$  photoproduction cross section. An analytical result has been derived for the double differential one-particle-inclusive cross section  $d\sigma/dt_1 du_1$ . The corresponding expressions are however too long to be presented here.

## 4 The parton cross section

The perturbative expansion of the total photon-parton cross section can be expressed in terms of scaling functions,

$$\hat{\sigma}_{i\gamma}(s, m_c^2) = \frac{\alpha\alpha_s^2 e_c^2}{m_c^2} \frac{|\varphi(0)|^2}{m_c^3} \left[ c_{i\gamma}^{(0)}(\eta) + 4\pi\alpha_s \left\{ c_{i\gamma}^{(1)}(\eta) + \bar{c}_{i\gamma}^{(1)}(\eta) \ln \frac{Q^2}{m_c^2} + \frac{\beta_0(n_{\text{lf}})}{8\pi^2} c_{i\gamma}^{(0)}(\eta) \ln \frac{\mu_R^2}{Q^2} \right\} \right], \quad (30)$$

where  $i = g, q, \bar{q}$  denote the parton targets and  $\beta_0(n_{\text{lf}}) = (11N - 2n_{\text{lf}})/3$ . The scaling functions depend on the energy variable  $\eta = s/4m_c^2 - 1$ .  $c_{i\gamma}^{(0)}$  is the lowest-order contribution which scales  $\sim \eta^{-1} \sim 4m_c^2/s$  asymptotically. The cross section is put into a form in which the renormalization scale  $\mu_R$  and the factorization scale  $Q$  can be varied independently. The scaling functions  $c_{i\gamma}(\eta)$  are shown in Figs.6(a) and (b) for the parton cross sections integrated over  $z \leq z_1$  where we have chosen  $z_1 = 0.9$  as discussed before. [Note that the definition of  $z$  is the same at the nucleon and parton level since the momentum fraction  $x$  of the partons cancels in the ratio  $z = p \cdot k_\psi / p \cdot k_\gamma$ .] In Fig.7 the scaling function of the gluon initiated parton process has been decomposed into a "virtual + soft" (V+S) piece and a "hard" (H) gluon-radiation piece. The  $\ln^i \Delta$  singularities of the (V+S) cross sections are mapped into (H), cancelling the equivalent logarithms in this contribution so that the limit  $\Delta \rightarrow 0$  can safely be carried out. The nomenclature "hard" and "virtual + soft" is therefore a matter of definition, and negative values of  $c^{(\text{H})}$  may occur in some regions of the parameter space. [In the range  $0.2 \lesssim \eta \lesssim 2$  the hard gluon-radiation piece  $c_{g\gamma}^{(1,\text{H})}$  as well as  $\bar{c}_{g\gamma}^{(1)}$  differ from the curves in Ref.[28] by a few percent since the experimental cut  $z < 0.9$  was not implemented properly in one term of Ref.[28].]

The following comments can be inferred from the figures. (i) The form of the hard-gluon radiation piece  $c^{(\text{H})}$  resembles the corresponding scaling function in open-charm photoproduction [33]. The logarithmic enhancement near threshold can be attributed to initial state gluon bremsstrahlung. The "virtual + soft" contribution for  $J/\psi$  production is, however, significantly more negative than for open-charm production. The destructive interference with the lowest-order amplitude is not unplausible though, as the momentum transfer of virtual gluons has a larger chance [in a quasi-classical approach] to scatter quarks out of the small phase-space element centered at  $p_c + p_{\bar{c}} = p_{J/\psi}$  than to scatter them from outside into this small element. (ii) While  $c_{g\gamma}^{(0)}$  and  $c_{g\gamma}^{(1,\text{V+S})}$  scale asymptotically  $\sim 1/s$ , the hard coefficients  $c_{g\gamma}^{(1,\text{H})}$  and  $c_{q\gamma}^{(1)}$  [as well as  $\bar{c}_{g,q\gamma}^{(1)}$ ] approach plateaus for high energies, built-up by the flavour excitation mechanism. (iii) The cross sections on the quark targets are more than one order of magnitude smaller than those on the gluon target. (iv) A more detailed presentation of the spectra would reveal that the perturbative analysis is not under proper control in the limit  $z \rightarrow 1$ , as anticipated for this singular boundary region (see the detailed discussion in Sec.5). Outside the diffractive region, i.e. in the truly inelastic domain, the perturbation theory is well-behaved however.

## 5 The photon-proton cross section

The results for inelastic  $J/\psi$  production in photon-proton collisions

$$\gamma + P \rightarrow J/\psi + X \quad (31)$$

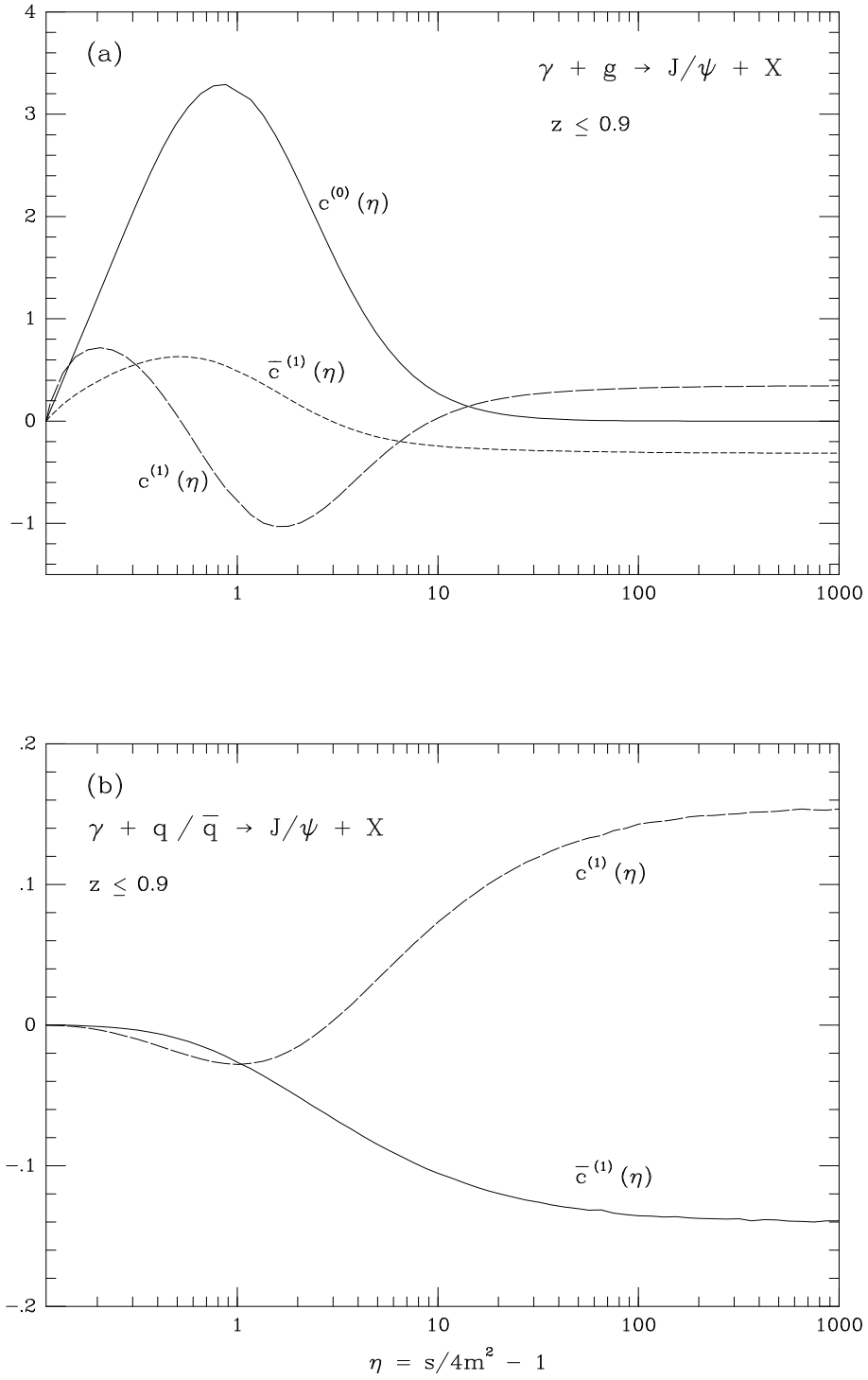


Figure 6: (a) Coefficients of the QCD corrected total inelastic [ $z \leq 0.9$ ] cross section  $\gamma+g \rightarrow J/\psi+X$  in the physically relevant range of the scaling variable  $\eta = s_{\gamma p}/4m^2 - 1$ ; and (b) for  $\gamma + q/\bar{q} \rightarrow J/\psi + X$ .

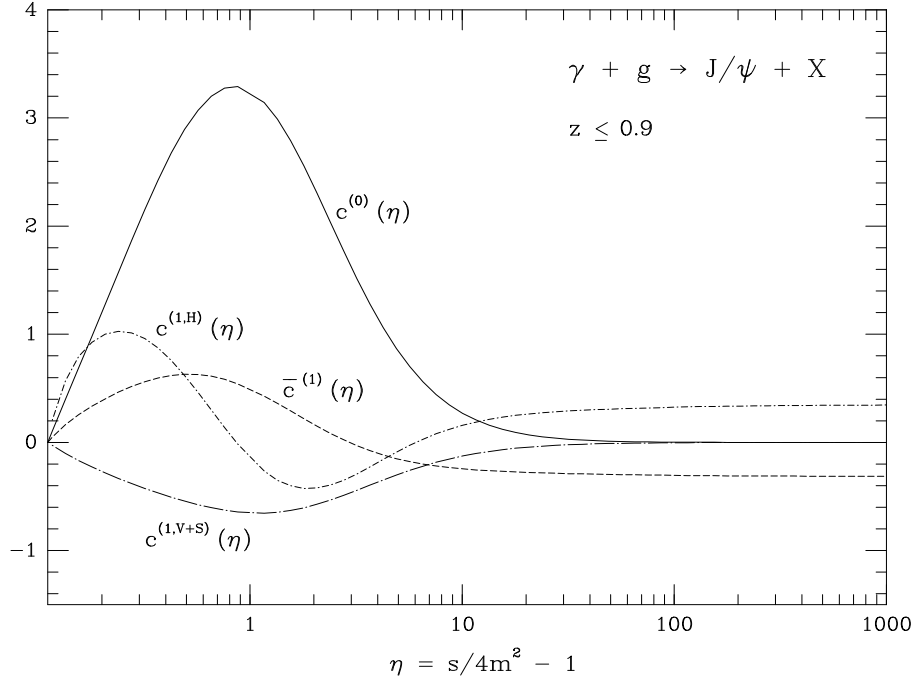


Figure 7: Coefficients of the QCD corrected total inelastic [ $z \leq 0.9$ ] cross section  $\gamma + g \rightarrow J/\psi + X$  split into a hard piece and a virtual plus soft piece.

are obtained from the partonic cross sections by convolution with the gluon and light-quark distributions  $f_i^P$  in the proton

$$d\sigma^{\gamma P} = \sum_{i=g,q(\bar{q})} \int dx f_i^P(x, Q^2) d\hat{\sigma}^{\gamma i} \quad . \quad (32)$$

In the following we present a comprehensive analysis of total cross sections and differential distributions for the energy range of the fixed-target experiments and for inelastic  $J/\psi$  photoproduction at HERA.

### 5.1 The energy range of the fixed target experiments

Inelastic  $J/\psi$  photoproduction has been measured in fixed-target experiments [20,21] at photon energies near  $E_\gamma = 100$  GeV, corresponding to invariant energies of about  $\sqrt{s_{\gamma p}} \approx 14$  GeV. Before comparing the theoretical predictions with the experimental data we will examine the effect of the next-to-leading order corrections in some detail.

In Figs.8 and 9 the  $J/\psi$  energy spectrum  $d\sigma/dz$  and the  $J/\psi$  transverse momentum distribution  $d\sigma/dp_\perp^2$  are shown at an initial photon energy of  $E_\gamma = 100$  GeV. The GRV parametrizations of the parton densities [45] have been adopted. They are particularly suited to characterize the magnitude of the radiative corrections since they allow one to compare the results for the Born cross section folded with leading-order parton densities, with the cross sections consistently evaluated for parton cross sections and parton densities in next-to-leading order. As the average momentum fraction of the partons  $\langle x \rangle \sim 0.1$  is moderate, the curves are not sensitive to the parametrization in the small- $x$  region. The renormalization scale has been identified with the factorization scale and set to  $\mu_R = Q = M_{J/\psi}$ . For  $\alpha_s$  the two-loop formula is used with  $n_{\text{lf}}$  active flavours and  $\Lambda_{\overline{\text{MS}}}^{(5)} = 215$  MeV, corresponding to the average fit value in Ref.[46]. Since the cross section depends strongly on the



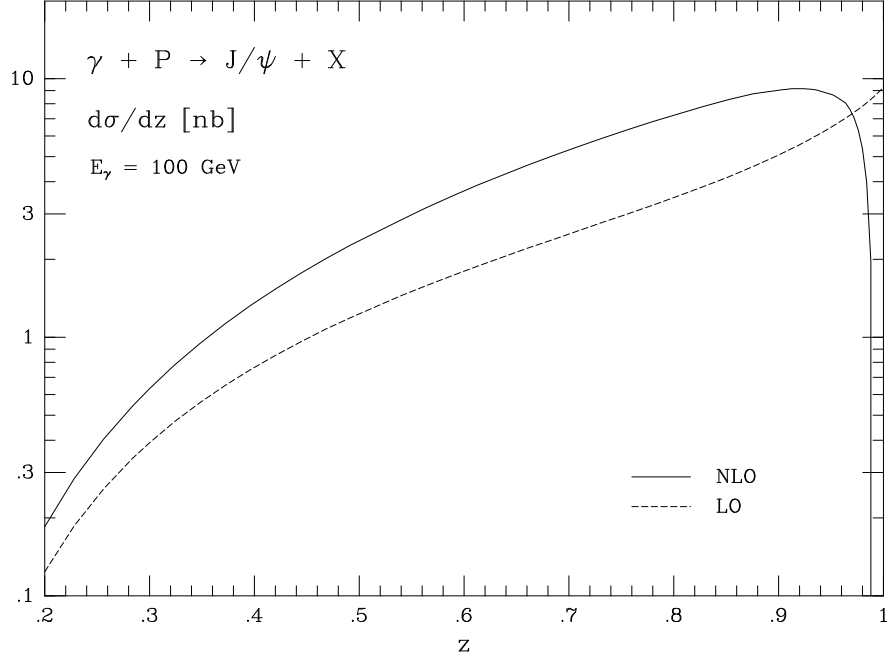


Figure 8: Energy distribution  $d\sigma/dz$  at an initial photon energy of  $E_\gamma = 100$  GeV.

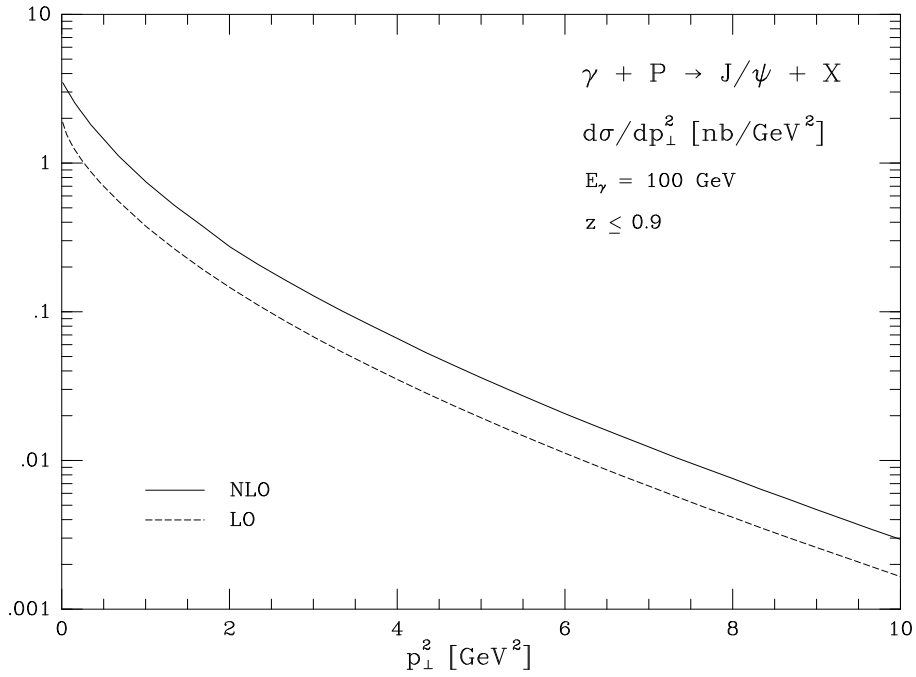


Figure 9: Transverse momentum distribution  $d\sigma/dp_\perp^2$  at an initial photon energy of  $E_\gamma = 100$  GeV integrated in the inelastic region  $z \leq 0.9$ .

QCD coupling, we adopt this measured value, thus allowing for a slight inconsistency to the extent that the GRV fits are based on a marginally lower value of  $\alpha_s$  (cf. Ref.[47]). In next-to-leading order, the wave-function at the origin is related to the leptonic  $J/\psi$  width by

$$\Gamma_{ee} = \left(1 - \frac{16}{3} \frac{\alpha_s}{\pi}\right) \frac{16\pi\alpha^2 e_c^2}{M_{J/\psi}^2} |\varphi(0)|^2 \quad (33)$$

with only transverse gluon corrections taken into account explicitly [48]. We use  $\Gamma_{ee} = 5.26$  keV,  $M_{J/\psi} = 3.097$  GeV [46] and  $m_c = M_{J/\psi}/2$ .

From Fig.8 one can infer that the perturbative QCD analysis is not under proper control in the limit  $z \rightarrow 1$ , as anticipated for this singular boundary region. If we restrict the analysis to the inelastic domain  $z \lesssim 0.9$  the perturbative expansion is well-behaved however and the next-to-leading order corrections do not strongly affect the shape of the distributions. The  $K$ -factor,  $K \equiv \sigma_{\text{NLO}}/\sigma_{\text{LO}}$ , is nearly independent of  $z$  and  $p_\perp$  in the inelastic region  $z \lesssim 0.9$ . Its magnitude turns out to be  $K \sim 2.0$  with one part  $\sim 1.73$  due to the QCD radiative corrections of the leptonic  $J/\psi$  width [48] and a second part  $\sim 1.2$  due to the dynamical QCD corrections. The slope of the transverse momentum distribution,  $d\sigma/dp_\perp^2 \propto \exp(-bp_\perp^2)$ , is predicted to be  $b \sim 0.6$  GeV $^{-2}$ , in good agreement with the experimental value  $b = 0.62 \pm 0.2$  GeV $^{-2}$  [20].

The scale dependence of the theoretical prediction is reduced considerably when higher-order QCD corrections are included. This is demonstrated in Fig.10 where we compare the scale dependence of the leading and next-to-leading order total cross section in the inelastic region  $z \leq 0.9$ .

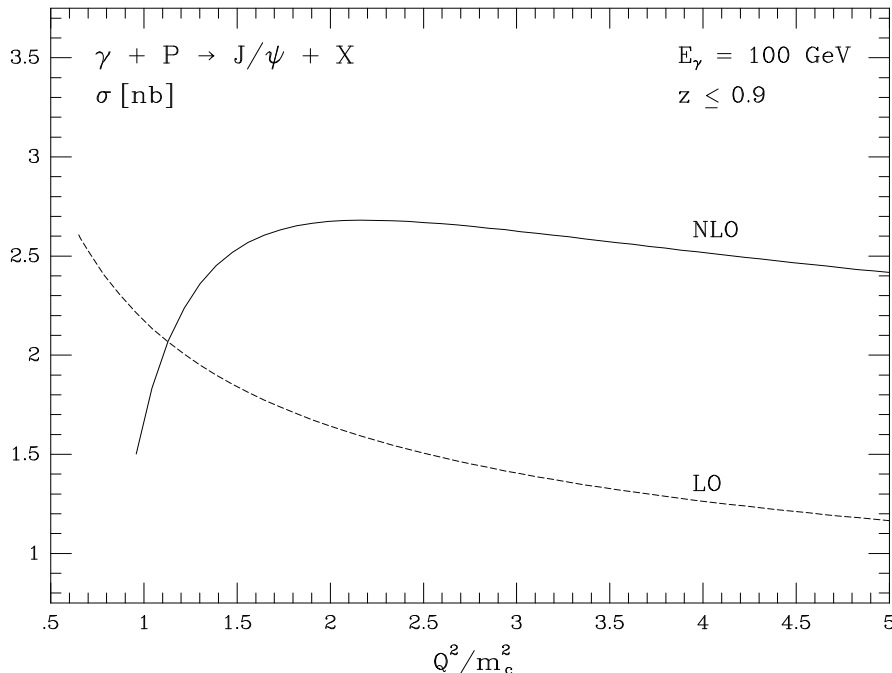


Figure 10: Dependence of the total cross section  $\gamma + P \rightarrow J/\psi + X$  on the renormalization/factorization scale  $Q$  at an initial photon energy of  $E_\gamma = 100$  GeV.

For the sake of simplicity, the renormalization scale has been identified with the factorization scale,  $\mu_R = Q$ . While the ratio of the cross sections in leading order for  $Q^2 = m_c^2 : (2m_c^2) : M_{J/\psi}^2$  is given by  $1.7 : 1.3 : 1$ , it is much closer to unity,  $0.7 : 1.1 : 1$ , in the next-to-leading order calculation. The cross section runs through a maximum [49] near  $Q^2 \approx 2m_c^2$  with broad width, the origin of the stable behaviour in  $Q$ .

The next-to-leading order predictions can be confronted with photoproduction data of the fixed target experiments. For a meaningful comparison, the theoretical uncertainties due to variation of the charm quark mass and the strong coupling have to be taken into account properly. In the static approximation the choice  $m_c = M_{J/\psi}/2$  is required for a consistent description of the bound state formation. A smaller mass value, however, is favoured to describe the charm quark creation in the hard scattering process [50]. The value of the heavy quark mass in the short distance amplitude is the main parameter controlling the normalization of the cross section. It is therefore appropriate to adopt charm masses below  $m_c = M_{J/\psi}/2$ , thus allowing for a slight correction in the bound state formation. Leading-order analyses of  $J/\psi$  production that go beyond the static limit and incorporate a non-vanishing binding energy, find an effective charm mass value of  $m_c = 1.43$  GeV [25], in fairly good agreement with potential model calculations [51]. In order to demonstrate the uncertainty due to the variation of the charm quark mass, the strong coupling and the renormalization/factorization scale the results will be shown for (i)  $m_c = M_{J/\psi}/2 \approx 1.55$  GeV with  $\Lambda_{\overline{\text{MS}}}^{(5)} = 215$  MeV and  $Q^2 = \mu_R^2 = M_{J/\psi}^2$  (as used in the previous figures) and (ii)  $m_c = 1.4$  GeV with  $\Lambda_{\overline{\text{MS}}}^{(5)} = 300$  MeV (corresponding to the  $1\sigma$  upper boundary of the error band in Ref.[46]) and  $Q^2 = \mu_R^2 = 2m_c^2$ .

In Fig.11 we confront the leading and next-to-leading order calculations with the  $J/\psi$  energy spectra measured at photon energies near  $E_\gamma = 100$  GeV [20,21]. It is clear from Fig.11 that

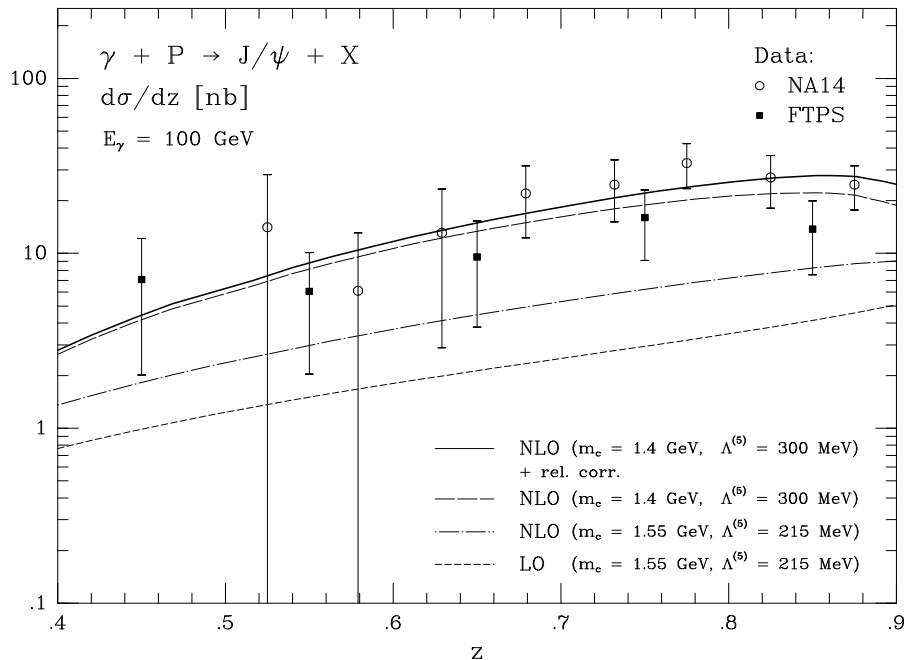


Figure 11: Energy spectrum  $d\sigma/dz$ , at the initial photon energy  $E_\gamma = 100$  GeV compared with the photoproduction data [20,21].

the variation of the charm mass and the strong coupling does not strongly affect the shape of the distribution but only results in some uncertainty concerning the overall normalization. In a systematic expansion one may finally add the relativistic corrections as estimated in Ref.[25].

The dependence of the total cross section  $\gamma + P \rightarrow J/\psi + X$  on the photon energy  $E_\gamma$  is presented in Fig.12, again for the two choices of parameters (i) and (ii) as defined above, together with the photoproduction data [20,21]. From the curves shown in Fig.12 we deduce that the QCD corrections are large at moderate photon energies, but decrease with increasing energies, a consequence of the

negative dip in the  $c^{(1)}$  scaling function of Fig.6.

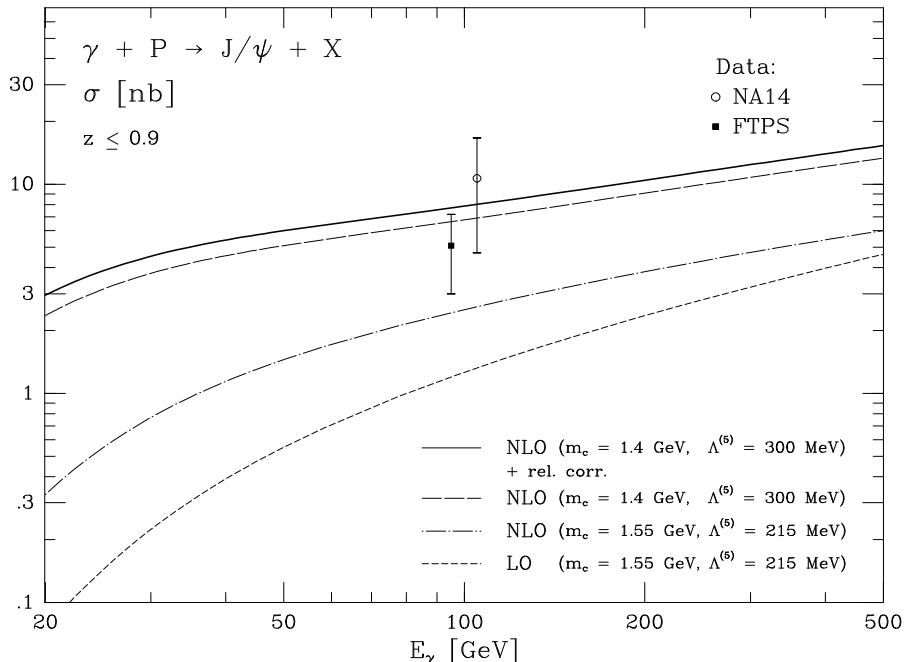


Figure 12: The total cross section [ $z \leq 0.9$ ] as a function of the initial photon energy.

Two conclusions can be drawn from the comparison of the next-to-leading order results with the experimental data. (i) The  $J/\psi$  energy dependence  $d\sigma/dz$  and the slope of the transverse momentum distribution  $d\sigma/dp_{\perp}^2$  are adequately accounted for by the theoretical prediction in the inelastic region. (ii) The absolute normalization of the cross section is somewhat less certain. However, taking into account the theoretical uncertainty due to variation of the charm quark mass and the strong coupling and allowing for higher-twist uncertainties of order  $(\Lambda/m_c)^k \lesssim 30\%$  for  $k \geq 1$ , we conclude that the normalization too appears to be under semi-quantitative control.

## 5.2 Inelastic $J/\psi$ photoproduction at HERA

The production of  $J/\psi$  particles in high energy  $ep$  collisions at HERA is dominated by photoproduction events where the electron is scattered by a small angle producing photons of almost zero virtuality. The measurements at HERA provide information on the dynamics of inelastic  $J/\psi$  photoproduction in a kinematical region very different from that available at fixed target experiments. The  $\gamma p$  centre of mass energies accessible at HERA are in the range  $30 \text{ GeV} \lesssim \sqrt{s_{\gamma p}} \lesssim 200 \text{ GeV}$ , corresponding to initial photon energies in a fixed-target experiment of  $450 \text{ GeV} \lesssim E_{\gamma} \lesssim 20,000 \text{ GeV}$ .

To begin with, we discuss the  $J/\psi$  energy spectrum  $d\sigma/dz$  and the  $J/\psi$  transverse momentum distribution  $d\sigma/dp_{\perp}^2$  at a typical HERA energy of  $\sqrt{s_{\gamma p}} = 100 \text{ GeV}$ . The parameters have been chosen as in the corresponding figures of Sec.5.1. From Figs.13 and 14 one can conclude that the next-to-leading order corrections are dominated by strong negative contributions in the limit  $z \rightarrow 1$  and  $p_{\perp} \rightarrow 0$ . This behaviour which has already been observed in the low energy region of the fixed-target experiments is much more pronounced in the high energy range at HERA. Even if the analysis is restricted to the region  $z \leq 0.8$  we still find that the fixed-order perturbative QCD calculation is not under proper control for  $p_{\perp} \rightarrow 0$ . This can be inferred from Fig.14 where the

transverse momentum spectrum is shown integrated in the range  $z \leq 0.9$  and  $z \leq 0.8$ , respectively.

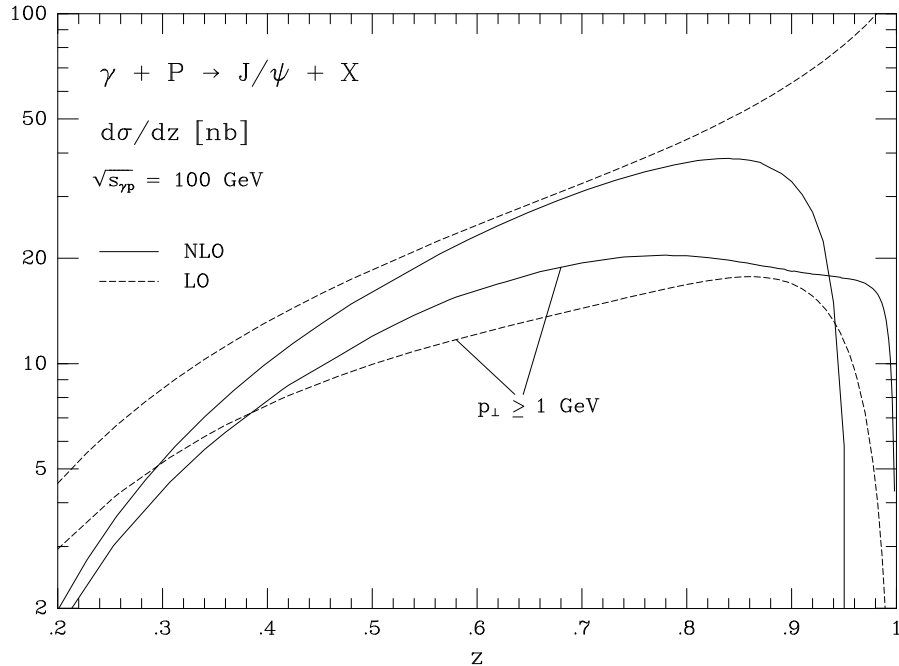


Figure 13: Energy distribution  $d\sigma/dz$  at the photon-proton centre of mass energy  $\sqrt{s_{\gamma p}} = 100$  GeV integrated in the full  $p_{\perp}$  range and in the restricted range  $p_{\perp} \geq 1$  GeV.

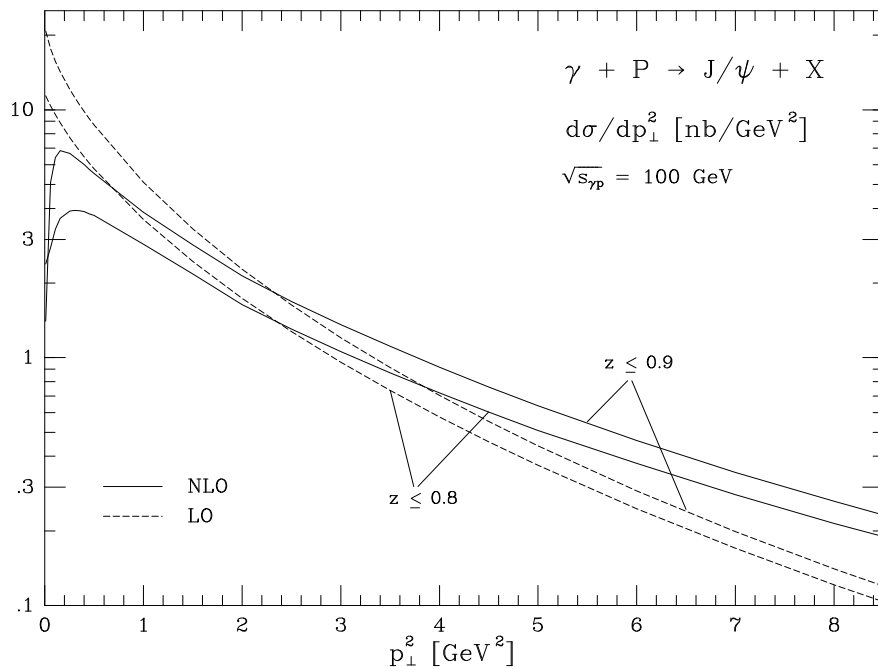


Figure 14: Transverse momentum distribution  $d\sigma/dp_{\perp}^2$  at the photon-proton centre of mass energy  $\sqrt{s_{\gamma p}} = 100$  GeV integrated in the region  $z \leq 0.9$  and  $z \leq 0.8$ .

For  $p_{\perp} \lesssim 0.5$  GeV the results of this calculation obviously require missing contributions from even higher orders in the perturbative expansion. No reliable prediction can be made in the small  $p_{\perp}$  and large  $z$  domain without resummation of large logarithmic corrections caused by multiple gluon

emission. It is therefore appropriate to exclude the region  $z \rightarrow 1$  and  $p_\perp \rightarrow 0$  from the analysis. In the following we will present the results in two kinematic domains, (I)  $z \leq 0.9$ , which is the minimal restriction in order to eliminate elastic/diffractive contributions, and (II)  $z \leq 0.8$  and  $p_\perp \geq 1$  GeV, which was found to be the region where fixed-order perturbation theory allows for a reliable prediction in the HERA energy range. The next-to-leading order results for the  $J/\psi$  energy spectrum are shown in Fig.13 integrated in the full  $p_\perp$  range and in the restricted range  $p_\perp \geq 1$  GeV. No singular behaviour is observed for the latter curve even in the limit  $z \rightarrow 1$ .

In Fig.15 we compare the scale dependence of the leading order and next-to-leading order total cross sections at the invariant energy  $\sqrt{s_{\gamma p}} = 100$  GeV. The renormalization scale has been

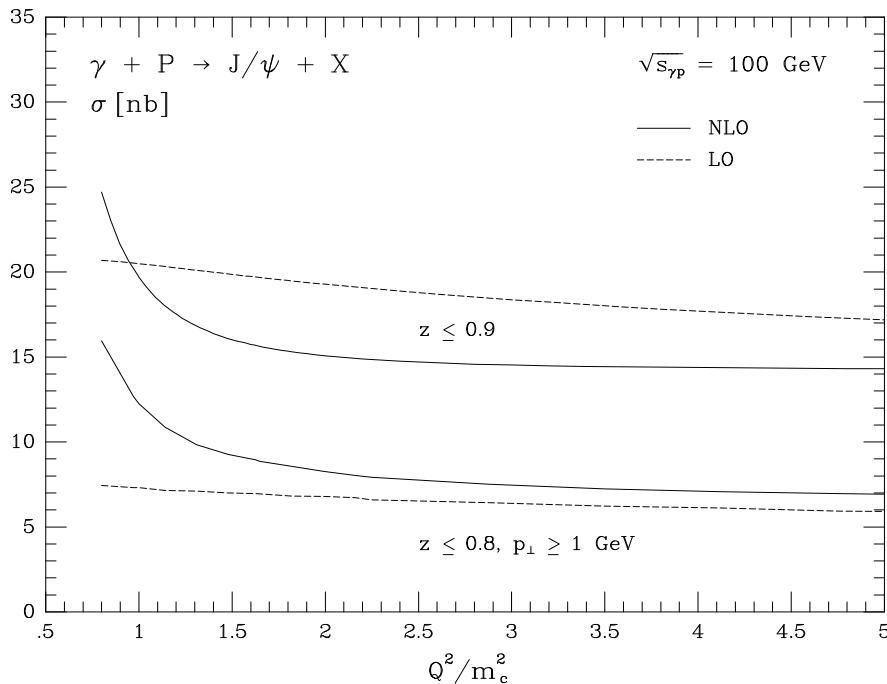


Figure 15: Dependence of the total cross section  $\gamma + P \rightarrow J/\psi + X$  on the renormalization/factorization scale  $Q$  at the photon-proton centre of mass energy  $\sqrt{s_{\gamma p}} = 100$  GeV. The results are shown in two kinematic domains: (I)  $z \leq 0.9$ ; (II)  $z \leq 0.8$  and  $p_\perp \geq 1$  GeV.

identified with the factorization scale,  $\mu_R = Q$ . The results are shown in the two kinematic domains (I)  $z \leq 0.9$  and (II)  $z \leq 0.8$  with  $p_\perp \geq 1$  GeV, as discussed above. From Fig.15 one can infer that the next-to-leading order result is insensitive to scale variations in an appreciable range near the reference scale  $\mu_R^2 = Q^2 = M_{J/\psi}^2$ . For scales below  $\mu_R^2 = Q^2 \sim M_{J/\psi}^2/2$  no stable prediction is possible. In contrast to the low energy region, the cross section in the HERA energy range does not exhibit a point of minimal scale sensitivity. In the BLM scheme [52] we find a value of  $\mu_R^2 \sim M_{J/\psi}^2/2$ . This scale is significantly larger than the corresponding BLM value for  $J/\psi$  decays. The typical kinematical energy scale is not set any more by the small gluon energy in the  $J/\psi$  decay but rather by the typical initial-state parton energies.

We will now present our final predictions for differential distributions and total cross sections for inelastic  $J/\psi$  photoproduction at HERA. In a systematic expansion we have added the relativistic corrections [25] which enhance the large  $z$  and small  $p_\perp$  region and thereby increase the total cross section integrated in the range  $z \leq 0.9$  by  $\approx 10\%$ . The inclusion of relativistic corrections does not change the results obtained in the more restricted domain  $z \leq 0.8$  and  $p_\perp \geq 1$  GeV. In order

to demonstrate the theoretical uncertainty the results are shown for (i)  $m_c = M_{J/\psi}/2 \approx 1.55$  GeV with  $\Lambda_{\overline{\text{MS}}}^{(5)} = 215$  MeV and  $Q^2 = \mu_R^2 = M_{J/\psi}^2$  (as used in the previous figures) and (ii)  $m_c = 1.4$  GeV with  $\Lambda_{\overline{\text{MS}}}^{(5)} = 300$  MeV and  $Q^2 = \mu_R^2 = 2m_c^2$ , as discussed in Sec.5.1. In Fig.16 we plot the transverse momentum distribution at the photon-proton centre of mass energy  $\sqrt{s_{\gamma p}} = 100$  GeV integrated in the region  $z \leq 0.9$  and  $z \leq 0.8$ . As could already be inferred from Fig.14, the inclusion of the

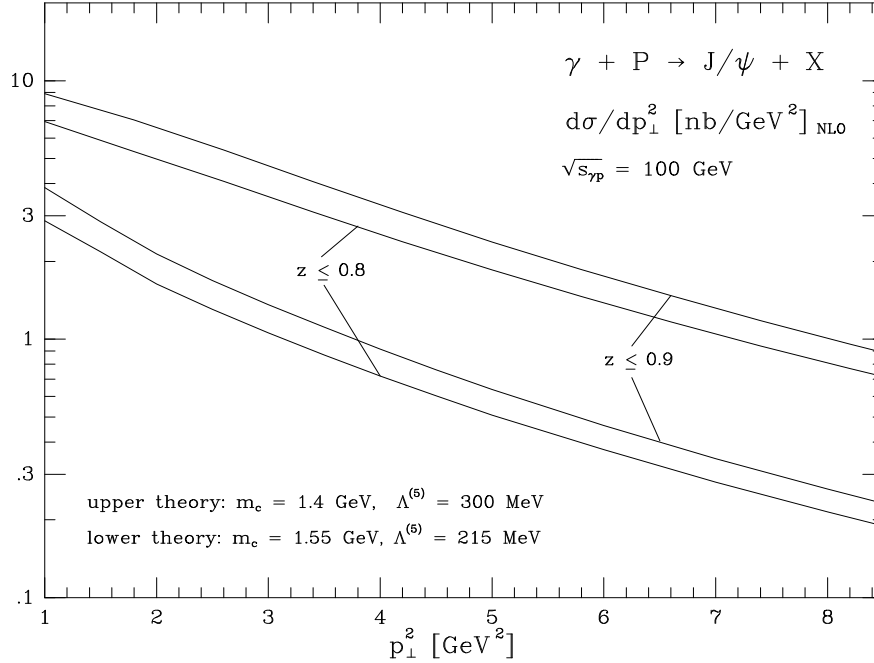


Figure 16: Transverse momentum distribution  $d\sigma/dp_{\perp}^2$  at the photon-proton centre of mass energy  $\sqrt{s_{\gamma p}} = 100$  GeV integrated in the region  $z \leq 0.9$  and  $z \leq 0.8$ .

next-to-leading order corrections increases the cross section in the range  $p_{\perp} \gtrsim 1$  GeV and results in a hardening of the distribution. For the slope,  $d\sigma/dp_{\perp}^2 \propto \exp(-bp_{\perp}^2)$ , we predict  $b \sim 0.3$  GeV $^{-2}$ . The  $J/\psi$  energy distribution is shown in Fig.17 integrated in the full  $p_{\perp}$  range and in the restricted range  $p_{\perp} \geq 1$  GeV, again for two choices of the charm quark mass and the strong coupling. In Figs.18(a) and (b) we plot the total cross section as a function of the photon-proton centre of mass energy in the HERA range. The results are shown in the two kinematic domains (I)  $z \leq 0.9$  and (II)  $z \leq 0.8$  with  $p_{\perp} \geq 1$  GeV. For domain (I), Fig.18(a), the  $K$ -factor is  $\sim 0.75$ , a consequence of the strong negative contribution present in the region  $p_{\perp} \rightarrow 0$ . In the more restricted kinematic domain (II), Fig.18(b), the next-to-leading order corrections significantly increase the cross section. For  $m_c = 1.4$  GeV with  $\Lambda_{\overline{\text{MS}}}^{(5)} = 300$  MeV and  $Q^2 = \mu_R^2 = 2m_c^2$ , we find  $K \equiv \sigma_{\text{NLO}}/\sigma_{\text{LO}} \approx 1.7$ .

An estimate of the cross section for inelastic photoproduction of  $\psi'$  particles can be obtained from the results presented here by replacing the leptonic decay width and multiplying with a phase space correction factor

$$\begin{aligned} \sigma(\gamma P \rightarrow \psi' X) &\approx \Gamma_{ee}^{\psi'}/\Gamma_{ee}^{J/\psi} (M_{J/\psi}/M_{\psi'})^3 \times \sigma(\gamma P \rightarrow J/\psi X) \\ &\approx 1/4 \times \sigma(\gamma P \rightarrow J/\psi X) \quad . \end{aligned} \quad (34)$$

The estimate (34) should be considered as a lower bound since it is based on a purely static approach. In the derivation of the phase space suppression factor  $(M_{J/\psi}/M_{\psi'})^3$  it is assumed that the effective charm masses in the short distance amplitudes scale like the corresponding  $\psi'$  and  $J/\psi$

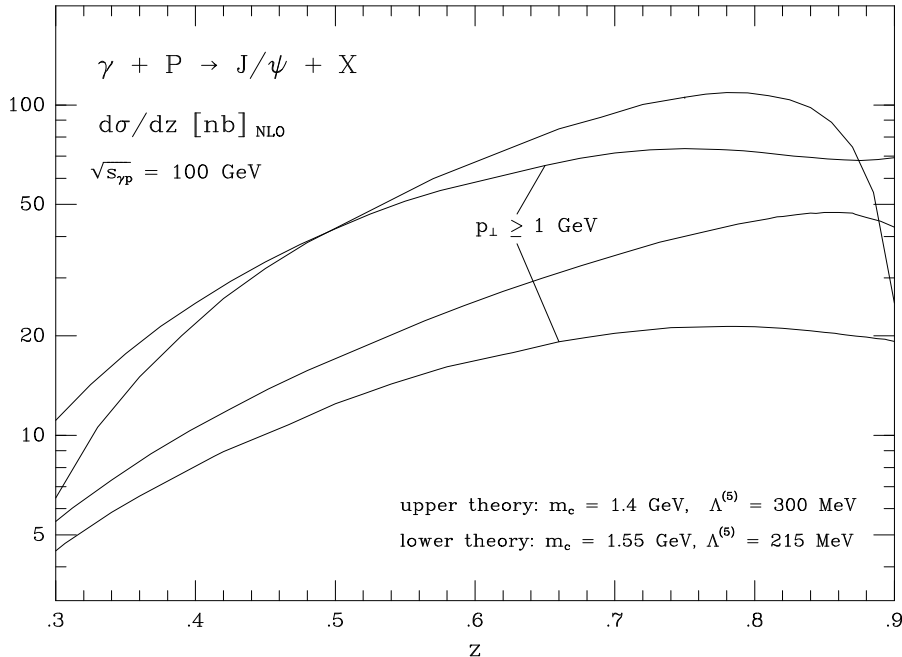


Figure 17: Energy distribution  $d\sigma/dz$  at the photon-proton centre of mass energy  $\sqrt{s_{\gamma p}} = 100$  GeV integrated in the full  $p_{\perp}$  range and in the restricted range  $p_{\perp} \geq 1$  GeV.

masses. This difference might be reduced by including relativistic corrections which are expected to be significantly larger for the  $\psi'$  state than for the  $J/\psi$  [51]. A measurement of the inelastic  $\psi'$  photoproduction cross section at HERA would clearly help to understand the impact of relativistic corrections on charmonium production.

The production of  $\Upsilon$  bottomonium bound states is suppressed, compared with  $J/\psi$  states, by a factor of about 300 at HERA, a consequence of the smaller bottom electric charge and the phase space reduction by the large  $b$  mass.

Since the momentum fraction of the partons at HERA energies is small, the cross sections presented above are sensitive to the parametrization of the gluon distribution in the small- $x$  region  $\langle x \rangle \sim 0.003$ . In Figs.19(a) and (b) we compare the next-to-leading order predictions for different parametrizations of the gluon distribution in the proton with first results measured at HERA [53,54]. We have used  $m_c = 1.4$  GeV with  $\Lambda_{\overline{\text{MS}}}^{(5)} = 300$  MeV and  $Q^2 = \mu_R^2 = 2m_c^2$ , as favoured by the low energy data. The data samples [53,54] contain background events from production of  $\psi'$  states with subsequent  $J/\psi$  decay [18]. This contribution has been included in the theoretical prediction, Figs.19(a) and (b), in order to allow for a meaningful comparison. According to (34) and the measured branching ratio  $\text{BR}(\psi' \rightarrow J/\psi X) = 57\%$  [46] the cascade production from  $\psi'$  states is conservatively expected to increase the cross section by  $\approx 15\%$ . For the parametrizations of the parton densities in the proton we have chosen four sets that are compatible with the recent HERA measurements of the proton structure functions [55]: the GRV parametrization [45], which has been adopted in all previous figures, the sets MRS(G), MRS(A') [56] and the CTEQ3 parametrization [57]. The difference in the small  $x$  behaviour of the gluon densities,  $xg \sim x^{-\lambda}$  where  $\lambda_{\text{GRV}} \approx 0.3-0.4$ ,  $\lambda_{\text{MRS(G)}} \approx 0.4$ ,  $\lambda_{\text{MRS(A')}} \approx 0.2$  and  $\lambda_{\text{CTEQ3M}} \approx 0.3$ , results in different normalizations and, to a smaller extend, in different shapes of the cross section as a function of the photon-proton centre of mass energy. The shape of the differential distributions in  $z$  and  $p_{\perp}$  is not very sensitive to changes



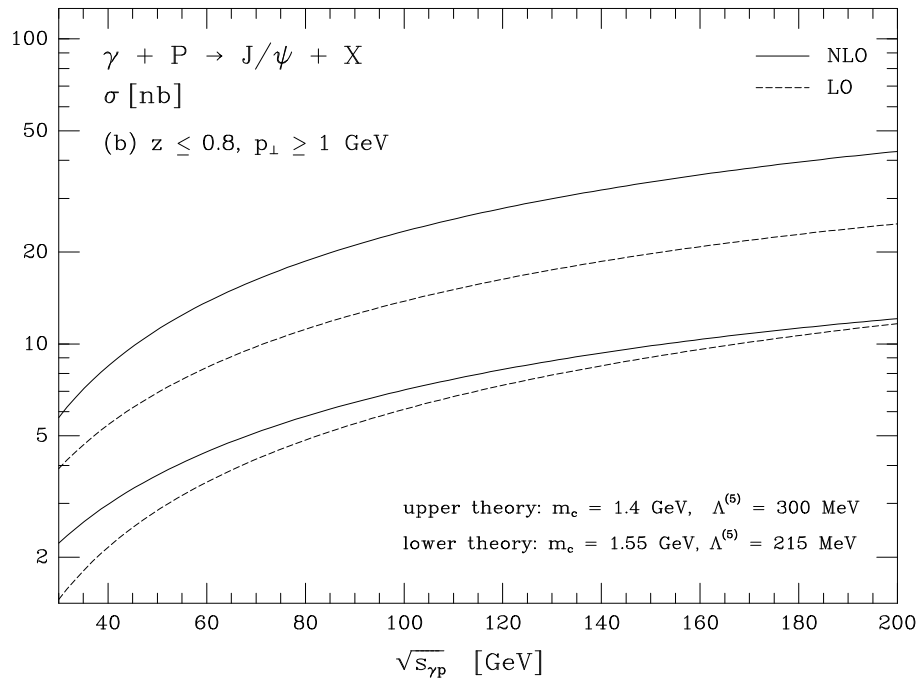
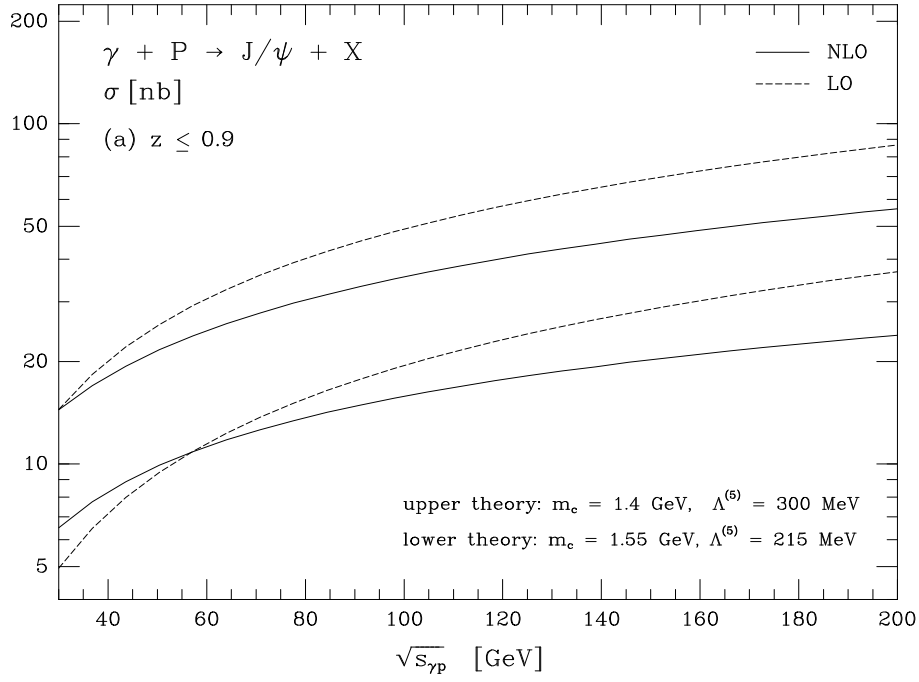


Figure 18: The total cross section for inelastic  $J/\psi$  photoproduction  $\gamma + P \rightarrow J/\psi + X$  as a function of the photon-proton centre of mass energy in the HERA energy range. The results are shown in two kinematic domains: (a)  $z \leq 0.9$ ; (b)  $z \leq 0.8$  and  $p_{\perp} \geq 1$  GeV.

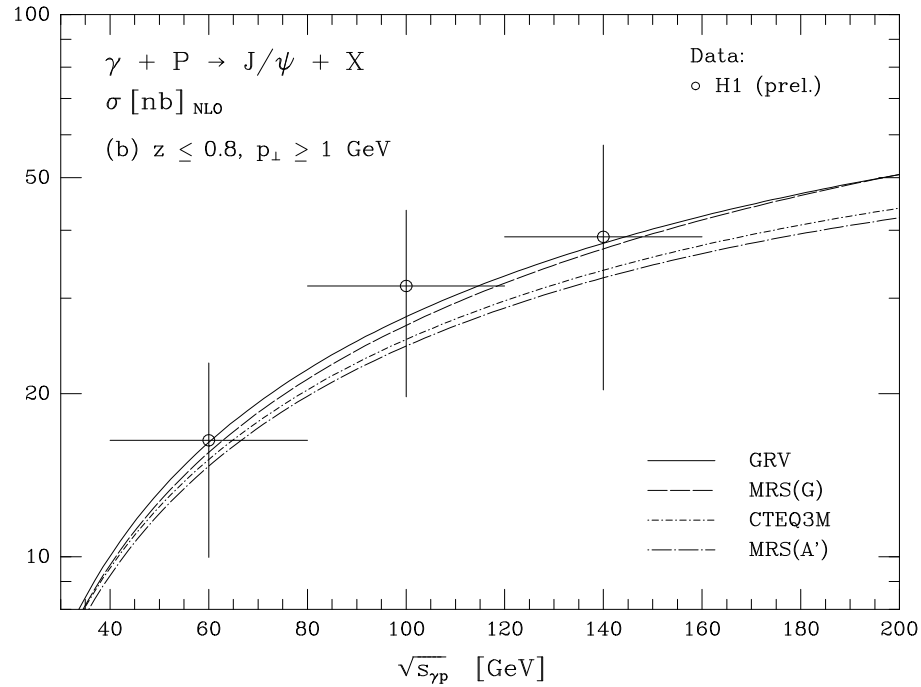
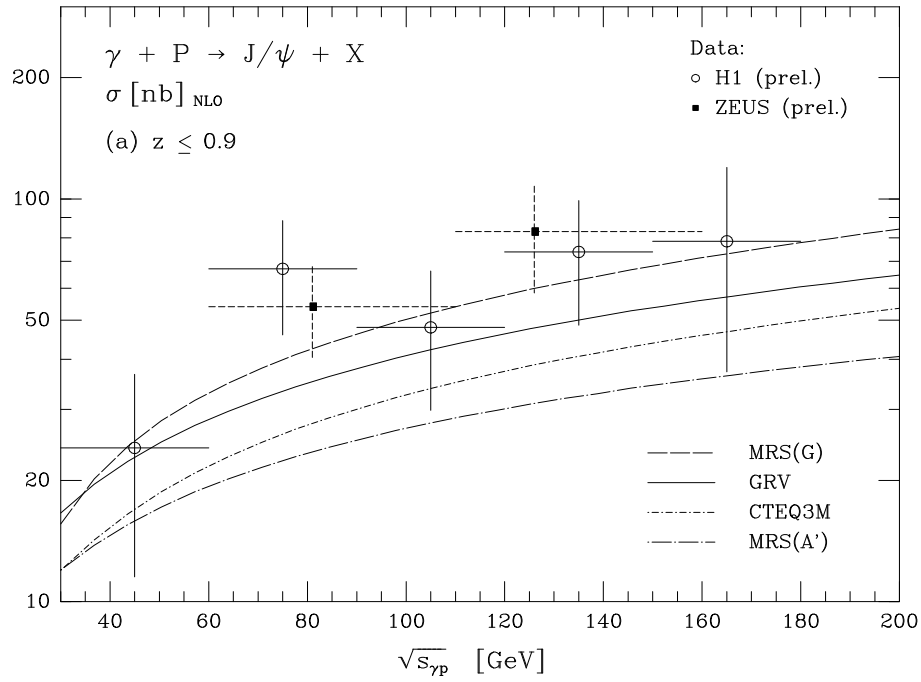


Figure 19: The total cross section as a function of the photon-proton centre of mass energy for different parametrizations of the gluon distribution of the proton compared with preliminary data from H1 [53] and ZEUS [54]. The results are shown in two kinematic domains: (a)  $z \leq 0.9$ ; (b)  $z \leq 0.8$  and  $p_{\perp} \geq 1 \text{ GeV}$ .

in the proton structure function. The theoretical result for the total cross section integrated in the kinematic domain  $z \leq 0.9$  on average underestimates the experimentally observed production rate, Fig.19(a). This could be anticipated since the perturbative analysis is not under proper control in the limit  $p_{\perp} \rightarrow 0$  and the next-to-leading order corrections are dominated by strong negative contributions for  $p_{\perp} \lesssim 0.5$  GeV, as shown in Fig.14. Following the arguments above, it is more adequate to compare theory and experiment in the kinematic domain  $z \leq 0.8$  and  $p_{\perp} \geq 1$  GeV, where fixed-order perturbation theory allows for a reliable prediction in the HERA energy range. This comparison is shown in Fig.19(b). It can be inferred from the plot that the next-to-leading order result not only accounts for the energy dependence of the cross section but also for the overall normalization. The sensitivity of the prediction to the gluon distribution in the proton is, however, not very distinctive in the more restricted domain  $z \leq 0.8$  and  $p_{\perp} \geq 1$  GeV. In particular the MRS(G) and GRV parton densities lead to almost identical results over the whole kinematical range accessible at HERA. A detailed analysis reveals that the size of the QCD corrections increases when adopting parton densities with flatter gluons. The sensitivity to different gluon distributions is thus reduced in next-to-leading order as compared to the leading-order result, in particular when choosing a small charm mass and a large value for the strong coupling. Parametrizations with extremely flat gluons like MRS(D0') [58] are clearly disfavoured by the recent HERA measurements of the proton structure function [55] and do not allow for a reliable prediction in the high energy region. For the parameters adopted in Fig.19(b), the MRS(D0') distribution leads to next-to-leading order results not very different from those obtained with the MRS(A') parametrization. The corresponding  $K$ -factors are however uncomfortably large,  $K \sim 4$ , casting doubts on the reliability of the perturbative expansion as obtained by using flat gluon distributions. If parton distributions with steep gluon densities are adopted, the next-to-leading order cross section is well-behaved and gives an adequate description of the experimental data, as demonstrated in Fig.19.

## 6 Conclusion

We have presented a complete calculation of the higher-order perturbative QCD corrections to inelastic photoproduction of  $J/\psi$  particles. In the energy range of the fixed target experiments,  $E_{\gamma} \sim 100$  GeV, including the next-to-leading order corrections reduces the scale dependence of the theoretical prediction and increases the cross section by about a factor of two. A comparison with photoproduction data of fixed-target experiments reveals that the  $J/\psi$  energy dependence and the slope of the transverse momentum distribution are adequately accounted for by the theoretical prediction in the inelastic region  $z \lesssim 0.9$ . Taking into account the uncertainty due to variation of the charm quark mass and the strong coupling and allowing for higher-twist effects of order  $(\Lambda/m_c) \lesssim 30\%$ , we conclude that the normalization too appears to be under semi-quantitative control. In the high energy range at HERA, a detailed analysis of the spectra has shown that the perturbative calculation is not well-behaved in the limit  $p_{\perp} \rightarrow 0$ . No reliable prediction can be made in this singular boundary region without resummation of large logarithmic corrections caused by multiple gluon emission. First experimental results from HERA indeed indicate that the production rate, obtained in the full  $p_{\perp}$  range, is on average underestimated by the theoretical predictions. If the small  $p_{\perp}$  region is excluded from the analysis, the next-to-leading order result not only accounts for the energy dependence of the cross section but also for the overall normalization. The results seem to favour a gluon density in the proton rising toward low  $x$ , consistent with recent measurements of the proton structure functions. Higher-twist effects must be included to improve

the quality of the theoretical analysis further.

### Acknowledgements

It is a pleasure to thank J. Zunft for a fruitful collaboration during earlier stages of this project and P.M. Zerwas for valuable advice, discussions and suggestions. I also thank J.G. Körner for comments and support. I have benefitted from helpful suggestions concerning technical aspects of the calculation by W. Beenakker and M. Spira and from discussions with M. Cacciari, M. Greco, R. Höpker, W. Kilian, J.H. Kühn, R. Rückl, W.J. Stirling, W.L. van Neerven and A. Vogt. I thank J. Stegborn for interesting conversations and comparison of part of the results. Last but not least, I would like to acknowledge discussions on experimental aspects of  $J/\psi$  photoproduction with S. Bertolin, R. Brugnera, H. Jung, B. Naroska, S. Schieck, G. Schmidt, R. Sell and L. Stanco.

## APPENDICES

### A The scalar integrals

Analytical results for the scalar integrals which emerge from the Passarino-Veltman reduction of the virtual amplitude are listed in this Appendix. The exchange of longitudinal gluons between the massive quarks in diagram Fig.3b leads to a Coulomb singularity  $\sim \pi^2/v$ , which appears in the evaluation of the corresponding loop integrals. The singularity has been isolated by introducing a small quark velocity  $v$ , as discussed in detail below. First, we will give the expressions for the Coulomb-finite integrals. The results are *not* analytically continued into the physical region

$$s, s_1 + 4m^2 \geq 4m^2, \quad t, t_1 + 4m^2 \leq 0, \quad u, u_1 + 4m^2 \leq 0 \quad , \quad (35)$$

with  $s_1, t_1$  and  $u_1$  as defined in (7). Therefore, the expressions for all permutations of the photon and gluon momenta can be obtained from the formulae listed below by interchanging  $t_1 \leftrightarrow u_1$ ,  $s_1 \leftrightarrow t_1$ , or  $s_1 \leftrightarrow u_1$ . Since any imaginary part of the integrals will disappear in the final result, only the real parts are given. The four-momenta are related by  $k_1 + k_2 = 2p + k_3$  and all particles are taken to be on-mass-shell,  $k_1^2 = k_2^2 = k_3^2 = 0$  and  $p^2 = m^2$ .

– The scalar one-point function is given by

$$A(m^2) = \mu^{4-n} \int \frac{d^n q}{(2\pi)^n} \frac{1}{q^2 - m^2} = iC_\epsilon m^2 \left[ \frac{1}{\epsilon} + 1 \right] \quad (36)$$

where

$$C_\epsilon = \frac{1}{16\pi^2} e^{-\epsilon(\gamma_E - \ln 4\pi)} \left( \frac{\mu^2}{m^2} \right)^\epsilon \quad (37)$$

and  $n = 4 - 2\epsilon$ .

– The scalar two-point function is defined by

$$B(p, m_1, m_2) = \mu^{4-n} \int \frac{d^n q}{(2\pi)^n} \frac{1}{[q^2 - m_1^2][(q+p)^2 - m_2^2]} \quad (38)$$

The following types of two-point functions appear in the calculation of the virtual amplitude:

$$B(k_1, 0, 0) = 0 \quad (39)$$

$$B(k_2 - k_3, 0, 0) = iC_\epsilon \left[ \frac{1}{\epsilon} - \ln \left( -\frac{t}{m^2} \right) + 2 \right] \quad (40)$$

$$B(p, 0, m) = B(2p, m, m) = iC_\epsilon \left[ \frac{1}{\epsilon} + 2 \right] \quad (41)$$

$$B(p - k_1, 0, m) = iC_\epsilon \left[ \frac{1}{\epsilon} + 2 - \frac{t_1}{t_1 + 2m^2} \ln \left( \frac{-t_1}{2m^2} \right) \right] \quad (42)$$

$$B(k_1 + k_2, m, m) = iC_\epsilon \left[ \frac{1}{\epsilon} + 2 + \beta \ln \left( \frac{1 - \beta}{1 + \beta} \right) \right] \quad (43)$$

Here and below we have used the shorthand notation  $\beta \equiv \beta(s) = \sqrt{1 - 4m^2/s}$ .

– The scalar three-point function is defined by

$$C(p_1, p_2, m_1, m_2, m_3) = \mu^{4-n} \int \frac{d^n q}{(2\pi)^n} \frac{1}{[q^2 - m_1^2][(q + p_1)^2 - m_2^2][(q + p_2)^2 - m_3^2]} \quad (44)$$

Eight different types of three-point functions appear in the virtual amplitude:

$$C(k_2, k_3, 0, 0, 0) = iC_\epsilon \frac{1}{t} \left[ \frac{1}{\epsilon^2} - \frac{1}{\epsilon} \ln \left( \frac{-t}{m^2} \right) + \frac{1}{2} \ln^2 \left( \frac{-t}{m^2} \right) - \frac{1}{2} \zeta(2) \right] \quad (45)$$

$$C(-k_3, -k_3 - p, 0, 0, m) = iC_\epsilon \frac{1}{s_1} \left[ \frac{1}{\epsilon^2} - \frac{2}{\epsilon} \ln \left( \frac{-s_1}{2m^2} \right) + 2 \ln^2 \left( \frac{-s_1}{2m^2} \right) + 2\text{Li}_2 \left( \frac{s_1 + 2m^2}{2m^2} \right) + \frac{1}{2} \zeta(2) \right] \quad (46)$$

$$C(k_3 - k_2, -p, 0, 0, m) = iC_\epsilon \frac{2}{t_1} \left[ \frac{1}{2} \ln^2 \left( -\frac{t}{2m^2} \right) + \text{Li}_2 \left( 1 - \frac{2m^2}{t} \right) + \text{Li}_2 \left( \frac{t}{4m^2} \right) - \text{Li}_2 \left( -\frac{2(2m^2 - t)}{t} \right) + \frac{5}{2} \zeta(2) \right] \quad (47)$$

$$C(-k_3, p - k_2, 0, 0, m) = iC_\epsilon \frac{2}{u_1 - t_1} \left[ \frac{1}{\epsilon} \ln \left( \frac{t_1}{u_1} \right) + \frac{1}{2} \ln^2 \left( \frac{-u_1}{2m^2} \right) - \frac{1}{2} \ln^2 \left( \frac{-t_1}{2m^2} \right) + \text{Li}_2 \left( 1 + \frac{2m^2}{t_1} \right) - \text{Li}_2 \left( 1 + \frac{2m^2}{u_1} \right) \right] \quad (48)$$

$$C(p, p - k_1, 0, m, m) = iC_\epsilon \frac{2}{t_1} \left[ -\text{Li}_2 \left( 1 + \frac{t_1}{2m^2} \right) + \zeta(2) \right] \quad (49)$$

$$C(p - k_1, -p - k_3, 0, m, m) = iC_\epsilon \frac{2}{s_1 - t_1} \left[ \text{Li}_2 \left( 1 + \frac{t_1}{2m^2} \right) - \text{Li}_2 \left( 1 + \frac{s_1}{2m^2} \right) \right] \quad (50)$$

$$C(-p, p + k_3, 0, m, m) = iC_\epsilon \frac{2}{s_1} \left[ \text{Li}_2 \left( 1 - \frac{s}{2m^2} \right) + \frac{1}{2} \zeta(2) - \text{Li}_2 \left( \frac{4m^2 - 2s}{4m^2 - s(1 + \beta)} \right) + \text{Li}_2 \left( \frac{4m^2}{4m^2 - s(1 + \beta)} \right) - \text{Li}_2 \left( \frac{4m^2 - 2s}{4m^2 - s(1 - \beta)} \right) + \text{Li}_2 \left( \frac{4m^2}{4m^2 - s(1 - \beta)} \right) \right] \quad (51)$$

$$C(k_1, k_1 + k_2, m, m, m) = -iC_\epsilon \frac{1}{s} \left[ \text{Li}_2 \left( \frac{2}{1+\beta} \right) + \text{Li}_2 \left( \frac{2}{1-\beta} \right) \right] , \quad (52)$$

where  $\zeta(2) = \pi^2/6$ .

– The scalar four-point function is defined by

$$D(p_1, p_2, p_3, m_1, m_2, m_3, m_4) = \mu^{4-n} \int \frac{d^n q}{(2\pi)^n} \frac{1}{[q^2 - m_1^2] [(q + p_1)^2 - m_2^2] [(q + p_2)^2 - m_3^2] [(q + p_3)^2 - m_4^2]} . \quad (53)$$

There are three different types of four-point functions:

$$D(k_2, k_3, -p + k_2, 0, 0, 0, m) = iC_\epsilon \frac{2}{tu_1} \left\{ \frac{3}{2} \frac{1}{\epsilon^2} - \frac{1}{\epsilon} \left[ 2 \ln \left( \frac{-u_1}{2m^2} \right) - \ln \left( \frac{-t_1}{2m^2} \right) + \ln \left( -\frac{t}{m^2} \right) \right] + 2 \ln \left( \frac{-u_1}{2m^2} \right) \ln \left( -\frac{t}{m^2} \right) - \ln^2 \left( \frac{-t_1}{2m^2} \right) - 2 \text{Li}_2 \left( 1 - \frac{t_1}{u_1} \right) - \frac{13}{4} \zeta(2) \right\} \quad (54)$$

$$D(-k_3, -p - k_3, p - k_2, 0, 0, m, m) = iC_\epsilon \frac{2}{s_1 t_1} \left\{ \frac{1}{\epsilon^2} + \frac{2}{\epsilon} \left[ \ln \left( \frac{-u_1}{2m^2} \right) - \ln \left( \frac{-t_1}{2m^2} \right) - \ln \left( \frac{-s_1}{2m^2} \right) \right] + 2 \ln^2 \left( \frac{-s_1}{2m^2} \right) + 2 \ln^2 \left( \frac{-t_1}{2m^2} \right) - 2 \ln^2 \left( \frac{-u_1}{2m^2} \right) + 4 \text{Li}_2 \left( \frac{u_1 - s_1}{t_1} \right) + 4 \text{Li}_2 \left( \frac{u_1 - t_1}{s_1} \right) - 4 \text{Li}_2 \left( \frac{u_1 - t_1}{s_1} \frac{u_1 - s_1}{t_1} \right) - \frac{3}{2} \zeta(2) \right\} \quad (55)$$

$$D(-p, -p + k_1, p + k_3, 0, m, m, m) = iC_\epsilon \frac{1}{t_1 s} \frac{4}{\lambda} \left\{ \text{Li}_2 \left( \frac{\lambda - 1}{\lambda + \beta} \right) + \text{Li}_2 \left( \frac{\lambda - 1}{\lambda - \beta} \right) - \text{Li}_2 \left( \frac{\lambda + 1}{\lambda + \beta} \right) - \text{Li}_2 \left( \frac{\lambda + 1}{\lambda - \beta} \right) \right\} \quad (56)$$

$$\text{where } \lambda \equiv \lambda(s_1, t_1) = \sqrt{\frac{s_1}{s_1 + 4m^2} \frac{t_1 + 4m^2}{t_1}} .$$

The five-point functions appearing in the calculation of the Feynman amplitudes shown in Fig.3(e,f) can be rewritten as linear combinations of the four-point integrals listed above.

In order to evaluate the Coulomb-singular diagrams shown in Fig.3(b) three five-point tensor integrals of the type

$$E_{0,\alpha,\alpha\beta,\alpha\beta\gamma,\alpha\beta\gamma\delta}(p_c, p_c - k_1, p_c - k_1 - k_2, -p_{\bar{c}}, 0, m, m, m, m) = \mu^{4-n} \int \frac{d^n q}{(2\pi)^n} \frac{1, q_\alpha, q_\alpha q_\beta, q_\alpha q_\beta q_\gamma, q_\alpha q_\beta q_\gamma q_\delta}{[q^2] [(q + p_c)^2 - m^2] [(q + p_c - k_1)^2 - m^2]} \times \frac{1}{[(q + p_c - k_1 - k_2)^2 - m^2] [(q - p_{\bar{c}})^2 - m^2]} \quad (57)$$

have to be calculated. The two additional integrals can be obtained from (57) by exchanging the photon and gluon momenta. The Coulomb singularity has been isolated by introducing a small

quark velocity  $v$  and the momenta  $p_c$  and  $p_{\bar{c}}$  fulfill the relations  $\vec{p}_c + \vec{p}_{\bar{c}} = \vec{0}$  and  $|\vec{p}_c - \vec{p}_{\bar{c}}| = mv$ . Since all loop integrals which have at least one power of the loop momentum  $q$  in the numerator are Coulomb-finite, the tensor reduction of (57) can be performed at  $v = 0$ . The  $\pi^2/v$  singularity is thus contained only in the scalar five-point integrals  $E_0$  and in four- and three-point functions of the type  $D(p_c, p_c - k_1, -p_{\bar{c}}, 0, m, m, m)$  and  $C(p_c, -p_{\bar{c}}, 0, m, m)$  which emerge from the tensor reduction. The integration of the three-point function is straightforward and we obtain in the static limit  $v \rightarrow 0$

$$C(p_c, -p_{\bar{c}}, 0, m, m) = -iC_\epsilon \frac{1}{2m^2} \left[ \frac{1}{\epsilon} + \frac{\pi^2}{v} - 2 \right] . \quad (58)$$

Alternatively, the Coulomb singularity (as well as the infrared pole) can be isolated by introducing a small gluon mass  $\lambda$ . In the limit  $\lambda \rightarrow 0$  one finds

$$C(p_c, -p_{\bar{c}}, 0, m, m) = -iC_\epsilon \frac{1}{2m^2} \left[ \ln \left( \frac{\lambda^2}{m^2} \right) + \frac{2\pi}{\lambda} m - 2 \right] \quad (59)$$

which shows the correspondence between the different regularization schemes (cf. Ref.[59]):

$$\begin{aligned} \ln \left( \frac{\lambda^2}{m^2} \right) &\iff \frac{1}{\epsilon} && \text{(IR-singularity)} \\ \frac{2\pi}{\lambda} m &\iff \frac{\pi^2}{v} && \text{(Coulomb-singularity)} \end{aligned} . \quad (60)$$

The singular piece of the four- and five point functions is determined by the infrared part of the integration region,  $q \rightarrow 0$ , and can thus be extracted by neglecting the loop momentum in the infrared finite propagators. In the limit  $|\vec{p}_c - \vec{p}_{\bar{c}}| = mv \rightarrow 0$  one finds for example

$$D^{(\text{IR})}(p_c, p_c - k_1, -p_{\bar{c}}, 0, m, m, m) = \frac{1}{[(p_c - k_1)^2 - m^2]} \frac{(-iC_\epsilon)}{2m^2} \left\{ \frac{1}{\epsilon} + \frac{\pi^2}{v} - 2 \right\} \quad (61)$$

and similar expressions for the other four- and five-point functions. No terms linear in  $v$  appear in the relativistic expansion of the coefficients multiplying the Coulomb-singular integrals. The corresponding expressions can thus be evaluated in the static limit  $v = 0$  from the start.

For the finite part of the four-point integral we obtain

$$\begin{aligned} D^{(\text{fin})}(p_c, p_c - k_1, -p_{\bar{c}}, 0, m, m, m) &\equiv \\ &D(p_c, p_c - k_1, -p_{\bar{c}}, 0, m, m, m) - \frac{1}{[(p_c - k_1)^2 - m^2]} C(p_c, -p_{\bar{c}}, 0, m, m) = \\ &iC_\epsilon \frac{2}{t_1 m^2} \left[ \frac{1}{\beta(t)} \ln \left( \frac{1 - \beta(t)}{1 + \beta(t)} \right) - \ln \left( \frac{2m^2}{t_1} \right) \right] . \end{aligned} \quad (62)$$

Similarly, the finite part of the five-point integral is given by

$$\begin{aligned} E^{(\text{fin})}(p_c, p_c - k_1, p_c - k_1 - k_2, p_{\bar{c}}, 0, m, m, m, m) &\equiv \\ &E(p_c, p_c - k_1, p_c - k_1 - k_2, p_{\bar{c}}, 0, m, m, m, m) \\ &- \frac{1}{[(p_c - k_1)^2 - m^2][(p_c - k_1 - k_2)^2 - m^2]} C(p_c, -p_{\bar{c}}, 0, m, m) \end{aligned} . \quad (63)$$

The difference  $E^{(\text{fin})} = E - E^{(\text{IR})}$  is infrared- and Coulomb-finite and a complete analytical result has been obtained. Since the corresponding expression is rather extensive we will only outline the

basic steps of the calculation. By using the Feynman parametrization technique one obtains

$$E = -\frac{i}{m^6} \left(\frac{\mu^2}{m^2}\right)^\epsilon \frac{\Gamma(3+\epsilon)}{(4\pi)^{n/2}} \mathcal{I} \quad , \quad (64)$$

where

$$\begin{aligned} \mathcal{I} = & \int_0^1 d\hat{x} \int_0^{1-\hat{x}} d\hat{y} \int_0^{1-\hat{x}-\hat{y}} d\hat{z} \int_0^{1-\hat{x}-\hat{y}-\hat{z}} d\hat{w} \left[ (\hat{x} - \hat{y} - \hat{z} - \hat{w})^2 - \hat{s}(1 - \hat{y} - \hat{z})\hat{y} \right. \\ & \left. - \hat{t}(1 + \hat{x} - \hat{y} - \hat{z} - \hat{w})(\hat{y} + \hat{z}) - \hat{u}(1 + \hat{x} - \hat{y} - \hat{z} - \hat{w})\hat{y} \right]^{-3-\epsilon} \end{aligned} \quad (65)$$

and

$$\hat{t} \equiv -\frac{2p \cdot k_1}{m^2}, \quad \hat{u} \equiv -\frac{2p \cdot k_2}{m^2}, \quad \hat{s} \equiv \frac{2k_1 \cdot k_2}{m^2} \quad . \quad (66)$$

Substituting

$$\hat{x} = x + y - 1, \quad \hat{y} = w, \quad \hat{z} = z - w, \quad \hat{w} = x - z, \quad (67)$$

we arrive at an expression which does not depend on the integration variable  $x$ :

$$\mathcal{I} = \int_0^1 dx \int_{1-x}^{2-2x} dy \int_0^x dz \int_0^z dw \left[ (1-y)^2 - \hat{t}yz - \hat{u}yw - \hat{s}w(1-z) \right]^{-3-\epsilon} \quad . \quad (68)$$

Interchanging the order of integration and evaluating two integrations, we find

$$\mathcal{I} = \frac{1}{2+\epsilon} \int_0^1 dz \int_0^z dy (y-z) \left[ f(\epsilon, \hat{s}, \hat{t}, \hat{u}, z, y) - 2f(\epsilon, \hat{s}, \hat{t}, \hat{u}, z, 2y) \right] \quad , \quad (69)$$

where

$$\begin{aligned} f(\epsilon, \hat{s}, \hat{t}, \hat{u}, z, y) \equiv & \frac{1}{\hat{u}y + \hat{s}z} \left\{ \left[ (1-y)^2 - (1-z)(y(\hat{t} + \hat{u}) + \hat{s}z) \right]^{-2-\epsilon} \right. \\ & \left. - \left[ (1-y)^2 - \hat{t}y(1-z) \right]^{-2-\epsilon} \right\} \quad . \end{aligned} \quad (70)$$

The singularity is contained in the expression

$$\mathcal{I}^S = \frac{1}{2+\epsilon} \int_0^1 dz \int_0^z dy (y-1) f^S(\epsilon, \hat{s}, \hat{t}, \hat{u}, z, y) \quad (71)$$

with

$$\begin{aligned} f^S(\epsilon, \hat{s}, \hat{t}, \hat{u}, z, y) \equiv & \frac{1}{\hat{u} + \hat{s}} \left\{ \left[ (1-y)^2 - (1-z)(\hat{t} + \hat{u} + \hat{s}) \right]^{-2-\epsilon} \right. \\ & \left. - \left[ (1-y)^2 - \hat{t}(1-z) \right]^{-2-\epsilon} \right\} \quad . \end{aligned} \quad (72)$$

The integration of  $\mathcal{I}^S$  is straightforward and we obtain

$$\begin{aligned} \mathcal{I}^S = & -\frac{1}{(1+\epsilon)} \frac{1}{(2+\epsilon)} \left[ -\frac{1}{\hat{t}(\hat{s} + \hat{t} + \hat{u})} \frac{1}{2\epsilon} + \frac{1}{\hat{s} + \hat{u}} \left\{ \frac{1}{\hat{t}} \ln \left( \frac{-\hat{t}}{1-\hat{t}} \right) \right. \right. \\ & \left. \left. - \frac{1}{\hat{s} + \hat{t} + \hat{u}} \ln \left( \frac{-\hat{s} - \hat{t} - \hat{u}}{1 - \hat{s} - \hat{t} - \hat{u}} \right) \right\} \right] \quad . \end{aligned} \quad (73)$$

The remaining difference

$$\begin{aligned} \mathcal{I}^{\text{fin}} = & \frac{1}{2} \int_0^1 dz \int_0^z dy \left[ (y-z) \left\{ f(\epsilon, \hat{s}, \hat{t}, \hat{u}, z, y) + 2f(\epsilon, \hat{s}, \hat{t}, \hat{u}, z, 2y) \right\} \right. \\ & \left. - (y-1) f^S(\epsilon, \hat{s}, \hat{t}, \hat{u}, z, y) \right] \end{aligned} \quad (74)$$

is finite and can be evaluated in the limit  $\epsilon \rightarrow 0$  by using elementary integration techniques.



## B The three-particle final states

In this Appendix we outline the kinematics for the processes involving three-particle final states and give explicit results for the infrared-collinear cross section.

### B.1 The phase space integration

For the calculation of the two-to-three-body processes (16), (17) and (21) we closely follow Ref.[35] and introduce the following 10 kinematical invariants:

$$\begin{aligned}
s &= (k_1 + k_2)^2 \equiv s_1 + 4m^2 & t_6 &= (k_3 - k_2)^2 \\
s_3 &= (k_3 + k_4)^2 & u_6 &= (k_3 - k_1)^2 \\
s_4 &= (2p + k_4)^2 - 4m^2 & u_1 &= (2p - k_2)^2 - 4m^2 \\
s_5 &= (2p + k_3)^2 - 4m^2 & t' &= (k_4 - k_1)^2 \\
t_1 &= (2p - k_1)^2 - 4m^2 & u' &= (k_4 - k_2)^2 \quad .
\end{aligned} \tag{75}$$

where  $k_1 + k_2 = 2p + k_3 + k_4$ . The invariants  $s$ ,  $t_1$  and  $u_1$  have already been defined in (7). Since we are dealing with a three-particle final state only five of the invariants are linearly independent. In the centre of mass frame of the outgoing light particles (gluons and/or light (anti-)quarks), the momenta are given by

$$\begin{aligned}
k_1 &= (\omega_1, \dots, 0, 0, \omega_1) \\
P_{J/\psi} = 2p &= (E_{J/\psi}, \dots, 0, p_{J/\psi} \sin \psi, p_{J/\psi} \cos \psi) \\
k_3 &= (\omega_3, \dots, -\omega_3 \sin \theta_1 \sin \theta_2, -\omega_3 \sin \theta_1 \cos \theta_2, -\omega_3 \cos \theta_1) \\
k_4 &= (\omega_4, \dots, \omega_3 \sin \theta_1 \sin \theta_2, \omega_3 \sin \theta_1 \cos \theta_2, \omega_3 \cos \theta_1) \\
k_2 &= (\omega_2, \dots, 0, p_{J/\psi} \sin \psi, p_{J/\psi} \cos \psi - \omega_1)
\end{aligned} \tag{76}$$

The coordinate axes can be chosen in such a way that the  $n - 4$  unspecified angular components do not contribute to the matrix element squared. From four-momentum conservation and the on-mass-shell constraints one can derive the identities

$$\begin{aligned}
\omega_1 &= \frac{s_1 + t_1 + 4m^2}{2\sqrt{s_3}}, & \omega_2 &= \frac{s_1 + u_1 + 4m^2}{2\sqrt{s_3}}, & \omega_3 = \omega_4 &= \frac{\sqrt{s_3}}{2} \\
E_{J/\psi} &= \frac{s_1 - s_3}{2\sqrt{s_3}}, & p_{J/\psi} &= \sqrt{E_{J/\psi}^2 - 4m^2}, & \cos \psi &= \frac{\omega_1^2 - \omega_2^2 + p_{J/\psi}^2}{2p_{J/\psi}\omega_1} \quad .
\end{aligned} \tag{77}$$

For the cross section one has

$$\begin{aligned}
\sigma &= \frac{1}{2!} K_C K_S \frac{1}{2s} \mu^{2(4-n)} \int \frac{d^n P_{J/\psi}}{(2\pi)^{n-1}} \int \frac{d^n k_3}{(2\pi)^{n-1}} \int \frac{d^n k_4}{(2\pi)^{n-1}} \delta^+(P_{J/\psi}^2 - 4m^2) \\
&\quad \times \delta^+(k_3^2) \delta^+(k_4^2) (2\pi)^n \delta^n(k_1 + k_2 - P_{J/\psi} - k_3 - k_4) |\mathcal{M}^R|^2,
\end{aligned} \tag{78}$$

$K_C$  and  $K_S$  denoting the colour and spin averaging factors. The factor  $1/2!$  has to be included for the two-gluon final states because of Bose symmetry. It is convenient to rewrite the cross section according to

$$\begin{aligned}
\sigma &= K_C K_S \frac{1}{2s} \frac{\mu^{2(4-n)}}{(2\pi)^{2n-3}} \int d^n P_{J/\psi} d^n \xi \delta^+(P_{J/\psi}^2 - 4m^2) \delta^n(k_1 + k_2 - P_{J/\psi} - \xi) \\
&\quad \times \frac{1}{2!} \int d^n k_3 \int d^n k_4 \delta^+(k_3^2) \delta^+(k_4^2) \delta^n(\xi - k_3 - k_4) |\mathcal{M}^R|^2 \quad .
\end{aligned} \tag{79}$$

The integral over the phase space of the two outgoing light partons is evaluated in the corresponding centre of mass frame:

$$\begin{aligned} \frac{1}{2!} \int d^n k_3 \int d^n k_4 \delta^+(k_3^2) \delta^+(k_4^2) \delta^n(\xi - k_3 - k_4) |M_R|^2 = \\ s_3^{(n-4)/2} \pi^{(n-4)/2} \frac{1}{4} \frac{\Gamma(\frac{n}{2} - 1)}{\Gamma(n-3)} \frac{1}{2} \int_0^\pi d\theta_1 \sin^{n-3} \theta_1 \int_0^\pi d\theta_2 \sin^{n-4} \theta_2 |\mathcal{M}^R|^2 \quad . \end{aligned} \quad (80)$$

The remaining integrations are performed in the centre of mass frame of the initial state particles with momenta given by

$$\begin{aligned} k_1 &= \sqrt{s}/2 (1, \dots, 0, 0, 1) \\ k_2 &= \sqrt{s}/2 (1, \dots, 0, 0, -1) \\ P_{J/\psi} &= (E_{J/\psi}, \dots, 0, p_{J/\psi} \sin \chi, p_{J/\psi} \cos \chi) \quad . \end{aligned} \quad (81)$$

One finds for the cross section

$$\begin{aligned} \sigma &= K_C K_S \frac{1}{s} \frac{(4\pi)^{-n} \mu^{2(4-n)}}{\Gamma(n-3)} \int dE_{J/\psi} (E_{J/\psi}^2 - 4m^2)^{\frac{n-3}{2}} \int_0^\pi d\chi \sin^{n-3} \chi \\ &\times s_3^{(n-4)/2} \frac{1}{2} \int_0^\pi d\theta_1 \sin^{n-3} \theta_1 \int_0^\pi d\theta_2 \sin^{n-4} \theta_2 |\mathcal{M}^R|^2 \quad . \end{aligned} \quad (82)$$

After changing the integration variables  $(E_{J/\psi}, \chi) \rightarrow (t_1, u_1)$  using

$$E_{J/\psi} = -\frac{t_1 + u_1}{2\sqrt{s}}, \quad \cos \chi = \frac{t_1 - u_1}{\sqrt{(t_1 + u_1)^2 - 16m^2s}} \quad (83)$$

we finally obtain

$$\begin{aligned} s^2 \frac{d^2\sigma}{dt_1 du_1} &= K_C K_S \frac{(4\pi)^{-n} \mu^{4-n}}{2\Gamma(n-3)} \left( \frac{t_1 u_1 - 4m^2 s}{\mu^2 s} \right)^{(n-4)/2} \\ &\times s_3^{(n-4)/2} \frac{1}{2} \int_0^\pi d\theta_1 \sin^{n-3} \theta_1 \int_0^\pi d\theta_2 \sin^{n-4} \theta_2 |\mathcal{M}^R|^2 \quad . \end{aligned} \quad (84)$$

The kinematical limits on  $t_1, u_1$  can be deduced from the constraints  $-1 \leq \cos \chi \leq 1$  and  $s_3 \geq 0$ :

$$-s \leq t_1 \leq -4m^2, \quad -s_1 - t_1 - 8m^2 \leq u_1 \leq \frac{4m^2 s}{t_1} \quad . \quad (85)$$

To perform the angular integrations the matrix element squared has been decomposed into sums of terms which have at most two factors containing the dependence on the polar angle  $\theta_1$  and the azimuthal angle  $\theta_2$ . This partial fractioning exploits the kinematical relations between the invariants defined in (75):

$$\begin{aligned} s_3 &= -u_6 - t_6 - s_5 \\ s_4 &= s_1 + u_6 + t_6 \\ s_5 &= -t_1 - u_1 - s_4 - 8m^2 \\ t_6 &= -u_1 - s_1 - u' - 4m^2 \\ u_6 &= -t_1 - s_1 - t' - 4m^2 \quad . \end{aligned} \quad (86)$$

By using identities as e.g.

$$\frac{1}{s_5 t_6 (s_4 + t_1 + 2t')} = \frac{1}{u_1} \left( \frac{1}{s_5 t_6} - \frac{1}{t_6 (s_4 + t_1 + 2t')} - \frac{2}{s_5 (s_4 + t_1 + 2t')} \right) \quad (87)$$

the angular integration can be reduced to the evaluation of standard integrals of the form

$$I_n^{(k,l)} = \int_0^\pi d\theta_1 \sin^{n-3} \theta_1 \int_0^\pi d\theta_2 \sin^{n-4} \theta_2 \times (a + b \cos \theta_1)^{-k} (A + B \cos \theta_1 + C \sin \theta_1 \cos \theta_2)^{-l} . \quad (88)$$

The results for these integrals can be found in Ref.[35].

## B.2 The infrared-collinear cross section

The calculation of the infrared-collinear cross section (20) will be outlined in this Appendix. The resulting expressions contain all divergences due to soft gluon emission and splitting of the final state gluon into gluon and light quark-antiquark pairs.

We begin by considering the infrared region of phase space where one of the final state gluon momenta  $k_{3,4}$  becomes soft. In the limit  $k_4 \rightarrow 0$  the amplitude of the real gluon emission factorizes into an eikonal factor multiplying the Born amplitude:

$$|\mathcal{M}^R|^2 \Big|_{k_4 \rightarrow 0} = \frac{-2k_2 \cdot k_3}{s_3 u'} g^2 \frac{1}{2} (f^{abc})^2 |\mathcal{M}^B|^2 \Big|_{Tr^2(T^a T^b)=1} , \quad (89)$$

and analogous for  $k_3 \rightarrow 0$

$$|\mathcal{M}^R|^2 \Big|_{k_3 \rightarrow 0} = \frac{-2k_2 \cdot k_4}{s_3 t_6} g^2 \frac{1}{2} (f^{abc})^2 |\mathcal{M}^B|^2 \Big|_{Tr^2(T^a T^b)=1} , \quad (90)$$

where  $(f^{abc})^2 = N(N^2 - 1)$ .

In addition to the soft gluon divergences, the amplitudes for the  $2 \rightarrow 3$  processes contain terms which are singular when the two outgoing light partons become collinear,  $k_3 \parallel k_4$ , i.e.  $\cos \theta_{34} \equiv \cos \theta = 1$ . For the calculation of the collinear matrix element we choose the four-momenta in the centre of mass frame of the incoming partons according to

$$\begin{aligned} k_1 &= \frac{\sqrt{s}}{2} (1, \dots, \sin \chi, 0, \cos \chi) \\ k_2 &= \frac{\sqrt{s}}{2} (1, \dots, -\sin \chi, 0, -\cos \chi) \\ k_3 &= \omega_3 (1, \dots, 0, 0, 1) \\ k_4 &= \omega_4 (1, \dots, \sin \theta \cos \phi, \sin \theta \sin \phi, \cos \theta) \\ P = 2p &= (E, \dots, -\omega_4 \sin \theta \cos \phi, -\omega_4 \sin \theta \sin \phi, -\omega_4 \cos \theta - \omega_3) . \end{aligned} \quad (91)$$

Hence, in the limit  $\theta \rightarrow 0$  the condition  $s_3 < \Delta$  is given by

$$s_3 = 2\omega_3\omega_4 (1 - \cos \theta) \approx \omega_3\omega_4 \theta^2 < \Delta . \quad (92)$$

When integrated over the solid angle

$$d\Omega \propto d\theta \sin^{n-3} \theta \approx \theta^{n-3} d\theta , \quad (93)$$

the  $1/s_3 \sim 1/\theta^2$  terms in the matrix element squared lead to logarithmic singularities in the limit  $\theta \rightarrow 0$ . The pieces with additional powers of  $\theta$  in the numerator only give contributions of the  $\mathcal{O}(\Delta)$  which vanish in the limit  $\Delta \rightarrow 0$ . Accordingly, all invariants in the expressions multiplying

the  $1/s_3$  propagator can be replaced by their values at  $\theta = 0$ :

$$\begin{aligned}
s_3^0 &= 0 & u^0 &= z(t_1 + 4m^2) \\
s_4^0 &= zs_1 & t_6^0 &= (1-z)(t_1 + 4m^2) \\
s_5^0 &= (1-z)s_1 & u_6^0 &= (1-z)(u_1 + 4m^2) \\
t^0 &= z(u_1 + 4m^2) & &
\end{aligned} \tag{94}$$

The other invariants remain unaltered. The splitting parameter  $z$  is defined as

$$z = \frac{\omega_4}{\omega_3 + \omega_4} \tag{95}$$

and should not be confused with the  $J/\psi$  energy variable defined in (2). The parts of the matrix element squared which are proportional to  $1/s_3^2 \sim 1/\theta^4$  have to be expanded up to the  $\mathcal{O}(\theta^2)$ . Gauge invariance ensures that in the resulting expression all terms  $\sim 1/\theta^4$  cancel. The contributions  $\sim \theta/\theta^4$  are proportional to  $\cos\phi$  and vanish after the azimuthal integration. The parts  $\sim \theta^2/\theta^4$  finally contribute to the collinear matrix element and lead to logarithmic singularities when integrated over the solid angle (93).

For the process  $\gamma g \rightarrow J/\psi + gg$  we obtain the following result for the matrix element squared in the limit  $\theta \rightarrow 0$ :

$$\begin{aligned}
&\int_0^\pi d\phi \sin^{n-4}\phi |\mathcal{M}^R|^2 \Big|_{\theta \rightarrow 0} = \\
&B\left(\frac{n-3}{2}; \frac{1}{2}\right) \frac{1}{6} P_{gg}(z) \frac{1}{s_3} g^2 (f^{abc})^2 |\mathcal{M}^B|^2 \Big|_{Tr^2(T^a T^b)=1} + \mathcal{O}\left(\frac{1}{\theta}\right) \quad , \tag{96}
\end{aligned}$$

where  $B(x; y) = \Gamma(x)\Gamma(y)/\Gamma(x+y)$  is the Beta-function. The gluon-gluon splitting function  $P_{gg}$  is given by

$$P_{gg} = 6 \left[ \frac{1-z}{z} + \frac{z}{1-z} + z(1-z) \right] \tag{97}$$

As mentioned before, the terms of the order  $1/\theta$  which have not been included in (96) only give contributions of the  $\mathcal{O}(\Delta)$  and thus vanish in the limit  $\Delta \rightarrow 0$ .

The infrared-collinear region of phase space (92) is illustrated in the  $z$ - $\theta$ -plane in Fig.20. For

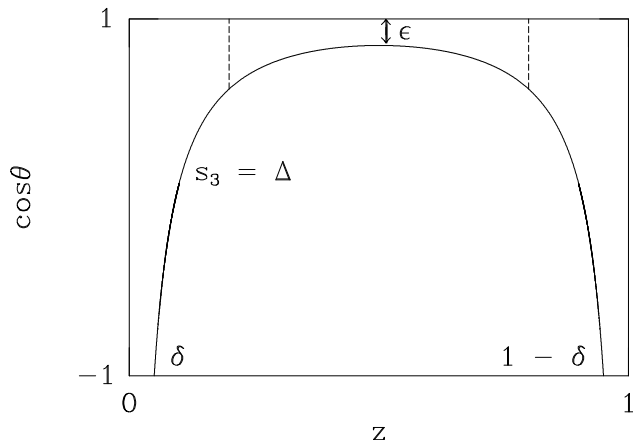


Figure 20: The infrared-collinear region of phase space in the  $z$ - $\theta$ -plane. The infrared parameter  $\delta$  and the collinear parameter  $\epsilon$  are obtained from  $s_3 = \Delta$  with  $s_3 \sim z(1-z)(1-\cos\theta)$  and vanish when  $\Delta \rightarrow 0$ .

$k_4 \rightarrow 0$  ( $z \rightarrow 0$ ) and  $k_3 \rightarrow 0$  ( $z \rightarrow 1$ ), the matrix element squared can be approximated by the expressions (89) and (90), respectively, while for  $\theta \rightarrow 0$  the collinear limit (96) has to be used. It is

clear from (89), (90) and (96) that in the infrared-collinear region, i.e. in the upper left and right corner in Fig.20, both approximations are identical.

In order to obtain a result for the matrix element squared in the region  $s_3 < \Delta$  which is Lorentz-frame independent, the splitting function  $P_{gg}$  of the collinear cross section can be rewritten in terms of invariant variables according to

$$\begin{aligned} \frac{1}{6}P_{gg}(z) &= \left[ \frac{1-z}{z} + \frac{z}{1-z} + z(1-z) \right] \\ &= \frac{k_2 \cdot k_3}{k_2 \cdot k_4} + \frac{k_2 \cdot k_4}{k_2 \cdot k_3} + \frac{(p \cdot k_3)(p \cdot k_4)}{[p \cdot (k_3 + k_4)]^2} + \mathcal{O}(\theta) \\ &= \frac{t_6}{u'} + \frac{u'}{t_6} + \frac{s_4 s_5}{(s_4 + s_5)^2} + \mathcal{O}(\theta) \quad . \end{aligned} \quad (98)$$

The expression (98) is Lorentz-invariant and can be used as an eikonal factor not only for the collinear configuration but also for the infrared region. Note that no additional divergences have been introduced in (98) since for  $k_2 \parallel k_4$  and  $k_2 \parallel k_3$  also the corresponding numerators vanish in the limit  $\theta \rightarrow 0$ ,  $k_2 \parallel k_3$  and  $k_2 \parallel k_4$ , respectively. Alternative ways of rewriting the splitting function in terms of invariants as e.g.

$$\frac{1-z}{z} = \frac{p \cdot k_3}{p \cdot k_4} + \mathcal{O}(\theta) \quad (99)$$

only approximate the collinear matrix element squared but can not be used to describe the infrared region.

An explicit distinction between collinear and infrared configurations as has been introduced in the centre of mass frame of the incoming partons according to (91) is no longer necessary. Using the invariant formulation for the matrix element squared in the region  $s_3 < \Delta$  as given by the eikonal factor (98), the phase space integrations necessary for the calculation of the corresponding cross section can conveniently be performed the centre of mass frame of the outgoing light partons:

$$\begin{aligned} &\int_0^\Delta ds_3 s_3^{-\epsilon} \int d\Omega_n \sum |\mathcal{M}^R|^2 \\ &= \int_0^\Delta ds_3 s_3^{-\epsilon} \int d\theta \sin^{n-3} \theta g^2 (f^{abc})^2 \\ &\quad \times B\left(\frac{n-3}{2}; \frac{1}{2}\right) \frac{1}{s_3} \left( \frac{t_6}{u'} + \frac{u'}{t_6} + \frac{s_4 s_5}{(s_4 + s_5)^2} \right) \sum |\mathcal{M}^B|^2 \Big|_{Tr^2(T^a T^b)=1} \\ &= 2\pi g^2 (f^{abc})^2 \frac{\Gamma(n-3)}{[\Gamma((n-2)/2)]^2} \left\{ 2B\left(\frac{n}{2}; \frac{4-n}{2}\right) + B\left(\frac{4-n}{2}, \frac{n}{2}\right) \right\} \\ &\quad \times \sum |\mathcal{M}^B|^2 \Big|_{Tr^2(T^a T^b)=1} \times \int_0^\Delta ds_3 s_3^{-1-\epsilon} \\ &= g^2 (f^{abc})^2 m^{2\epsilon} 4\pi \left(\frac{\Delta}{m^2}\right)^{-\epsilon} \left[ \frac{1}{\epsilon^2} + \frac{1}{\epsilon} \left(1 - \frac{1}{12}\right) + 2 - \frac{5}{36} \right] \sum |\mathcal{M}^B|^2 \Big|_{Tr^2(T^a T^b)=1} \quad . \end{aligned} \quad (100)$$

By using (20) and (100) one finally obtains for the cross section of the process  $\gamma g \rightarrow J/\psi + gg$  in the region  $s_3 < \Delta$ :

$$s^2 \frac{d\sigma}{dt_1 du_1} \Big|_{s_3 \leq \Delta} = \frac{1}{(N^2 - 1)} \frac{1}{4(1 - \epsilon)^2} \frac{\pi(4\pi)^{-2+\epsilon}}{\Gamma(1 - \epsilon)} \left( \frac{t_1 u_1 - 4m^2 s}{\mu^2 s} \right)^{-\epsilon} \delta(s_1 + t_1 + u_1 + 8m^2)$$

$$\begin{aligned}
& \times C_\epsilon g^2 (f^{abc})^2 \left[ \frac{1}{\epsilon^2} + \frac{1}{\epsilon} \left( 1 - \frac{1}{12} - \ln \frac{\Delta}{m^2} \right) + 2 - \frac{5}{36} \right. \\
& \left. + \frac{1}{2} \ln^2 \frac{\Delta}{m^2} - \frac{3}{2} \zeta(2) - \left( 1 - \frac{1}{12} \right) \ln \frac{\Delta}{m^2} \right] |\mathcal{M}^B|^2 \Big|_{Tr^2(T^a T^b)=1}
\end{aligned} \tag{101}$$

with  $C_\epsilon$  as defined in (37).

The collinear matrix element squared for the process  $\gamma g \rightarrow J/\psi + q\bar{q}$  is found to be

$$\begin{aligned}
& \int_0^\pi d\phi \sin^{n-4} \phi |\mathcal{M}^R|^2 \Big|_{\theta \rightarrow 0} = \\
& = B \left( \frac{n-3}{2}; \frac{1}{2} \right) P_{qg}(z) \frac{2}{s_3} g^2 |\mathcal{M}^B|^2 \Big|_{Tr^2(T^a T^b)=1} + \mathcal{O} \left( \frac{1}{\theta} \right) ,
\end{aligned} \tag{102}$$

with the gluon-(anti)quark splitting function  $P_{qg}$

$$P_{qg} = P_{\bar{q}g} = \frac{z^2 + (1-z)^2 - \epsilon}{1-\epsilon} . \tag{103}$$

By using the invariant expression

$$P_{qg} = P_{\bar{q}g} = \left[ \left( \frac{s_4}{s_1} \right)^2 + \left( \frac{s_5}{s_1} \right)^2 - \epsilon \right] \frac{1}{1-\epsilon} + \mathcal{O}(\theta) \tag{104}$$

we find for the cross section of the process  $\gamma g \rightarrow J/\psi + q\bar{q}$  in the region  $s_3 < \Delta$ :

$$\begin{aligned}
s^2 \frac{d\sigma}{dt_1 du_1} \Big|_{s_3 \leq \Delta} &= \frac{1}{(N^2-1)} \frac{1}{4(1-\epsilon)^2} \frac{\pi(4\pi)^{-2+\epsilon}}{\Gamma(1-\epsilon)} \left( \frac{t_1 u_1 - 4m^2 s}{\mu^2 s} \right)^{-\epsilon} \delta(s_1 + t_1 + u_1 + 8m^2) \\
&\times n_{\text{if}} C_\epsilon g^2 \frac{4}{3} \left( -\frac{1}{\epsilon} \right) \left[ 1 + \frac{5}{3} \epsilon - \epsilon \ln \frac{\Delta}{m^2} \right] |\mathcal{M}^B|^2 \Big|_{Tr^2(T^a T^b)=1} .
\end{aligned} \tag{105}$$

It has been checked explicitly that an expansion of the full matrix element squared in terms of small  $s_3$  leads to results identical to the equation above.

## C The kinematics of the photon-hadron cross section

In this Appendix we discuss the kinematics of the hadronic differential and total cross section. The single-particle inclusive hadronic cross section for the process

$$\gamma(K_1) + P(P_1) \rightarrow J/\psi(2p) + X \tag{106}$$

reads

$$S^2 \frac{d\sigma^{\gamma P}}{dT_1 dU_1} = \sum_{i=g,q(\bar{q})} \int_{x_{\min}}^1 \frac{dx}{x} f_i^P(x, Q^2) s^2 \frac{d\sigma^{\gamma i}}{dt_1 du_1} , \tag{107}$$

$f_g^P$  and  $f_{q(\bar{q})}^P$  denoting the parton distributions in the proton. The hadronic invariants are defined according to

$$\begin{aligned}
S &= (K_1 + P_1)^2 = s/x \\
T_1 &= (K_1 - 2p)^2 - 4m^2 = t_1 \\
U_1 &= (P_1 - 2p)^2 - 4m^2 = u_1/x .
\end{aligned} \tag{108}$$

From (108) and the kinematical condition  $xS + T_1 + xU_1 + 4m^2 \geq \Delta$  one deduces

$$x_{\min} = \frac{\Delta - T_1 - 4m^2}{S + U_1} . \quad (109)$$

It is convenient to rewrite the integration in terms of the  $J/\psi$  energy variable  $z$  (2) and the  $J/\psi$  transverse momentum  $p_\perp$ . By using the relations

$$s = xS \quad t_1 = -\frac{1}{z} (p_\perp^2 + 4m^2) \quad u_1 = -xzS \quad (110)$$

one finds

$$\frac{d\sigma^{\gamma P}}{dp_\perp^2 dz} = \sum_{i=g,q(\bar{q})} \int_{x_{\min}}^1 dx f_i^P(x, Q^2) \frac{xS}{z} \frac{d\sigma^{\gamma i}}{dt_1 du_1} , \quad (111)$$

where

$$x_{\min} = \frac{z\Delta + p_\perp^2 + 4m^2(1-z)}{Sz(1-z)} . \quad (112)$$

The total hadronic cross section is obtained by integration over  $p_\perp^2$  and  $z$ :

$$\sigma^{\gamma P}(S, m^2) = \int_{z_{\min}}^{z_{\max}} dz \int_{p_{\perp \min}^2}^{p_{\perp \max}^2} dp_\perp^2 \frac{d\sigma^{\gamma P}}{dp_\perp^2 dz}(S, p_\perp^2, z, m^2) , \quad (113)$$

with

$$\begin{aligned} z_{\max} &= 1 \\ z_{\min} &= 4m^2/S \\ p_{\perp \max}^2 &= (1-z)(Sz - 4m^2) - z\Delta \\ p_{\perp \min}^2 &= 0 . \end{aligned} \quad (114)$$

Finally, the  $p_\perp^2$  distribution is given by

$$\frac{d\sigma^{\gamma P}(S, p_\perp^2, m^2)}{dp_\perp^2} = \int_{z_{\min}}^{z_{\max}} dz \frac{d\sigma^{\gamma P}}{dp_\perp^2 dz}(S, p_\perp^2, z, m^2) , \quad (115)$$

where

$$z_{\min}^{\max} = \frac{(S + 4m^2 - \Delta)}{2S} \left( 1 \pm \sqrt{1 - \frac{4S(4m^2 + p_\perp^2)}{(S + 4m^2 - \Delta)^2}} \right) . \quad (116)$$

The cut-off parameter  $\Delta$  in the formulas above has to be included only for the calculation of the hard-gluon cross section. In our numerical program we have rewritten the  $\ln^i \Delta$  ( $i = 1, 2$ ) singularities of the virtual plus soft cross section as integrals over the momentum fractions of the partons  $x$ . The corresponding contributions have then been added to the hard cross section, cancelling the equivalent logarithms in this part so that the limit  $\Delta \rightarrow 0$  could safely be carried out.

## References

- [1] J.C. Collins, D.E. Soper, G. Sterman, Nucl. Phys. B263 (1986) 37.

- [2] G.A. Schuler, CERN-TH.7170/94 (1994), to appear in Phys. Rep.
- [3] H. Fritzsche, Phys. Lett. 67B (1977) 217; H. Fritzsche and K.H. Streng, Phys. Lett. 72B (1978) 385; M. Glück, J.F. Owens and E. Reya, Phys. Rev. D17 (1978) 2324; C.S. Kim and E. Reya, Phys. Lett. 300B (1993) 298.
- [4] E.L. Berger and D. Jones, Phys. Rev. D23 (1981) 1521.
- [5] R. Baier and R. Rückl, Phys. Lett. 102B (1981) 364.
- [6] J.G. Körner, J. Cleymans, M. Kuroda and G.J. Gounaris, Nucl. Phys. B204 (1982) 6; R. Baier and R. Rückl, Nucl. Phys. B208 (1982) 381, *ibid.* B218 (1983) 289, Z. Phys. C19 (1983) 251.
- [7] G.T. Bodwin, E. Braaten and G.P. Lepage, Phys. Rev. D51 (1995) 1125.
- [8] T. Mannel and G.A. Schuler, Phys. Lett. 349B (1995) 181.
- [9] W.E. Caswell and G.P. Lepage, Phys. Lett. 167B (1986) 437.
- [10] G.T. Bodwin, E. Braaten and G.P. Lepage, Phys. Rev. D46 (1992) R1914.
- [11] E. Braaten and S. Fleming, Phys. Rev. Lett. 74 (1995) 3327.
- [12] M. Cacciari, M. Greco, M.L. Mangano and A. Petrelli, CERN-TH/95-129; P. Cho and A.K. Leibovich, CALT-68-1988.
- [13] M. Vanttinen, P. Hoyer, S.J. Brodsky and W.K. Tang, Phys. Rev. D51 (1995) 3332; M. Vanttinen and W.K. Tang, SLAC-PUB-95-6931.
- [14] H. Jung, G.A. Schuler and J. Terrón, Int. J. Mod. Phys. A7 (1992) 7955; A. Ali, Proceedings, “XXI International Meeting on Fundamental Physics”, Madrid, 1993.
- [15] M.G. Ryskin, Z. Phys. C57 (1993) 89; J.R. Forshaw and M.G. Ryskin, Report DESY 94-162; J.R. Cudell, Nucl. Phys. B336 (1990) 1; A. Donnachie and P.V. Landshoff, Phys. Lett. 348B (1995) 213.
- [16] T. Ahmed et al. [H1 Collaboration], Phys. Lett. 338B (1994) 507.
- [17] A.D. Martin, C.-K. Ng and W.J. Stirling, Phys. Lett. 191B (1987) 200.
- [18] R. Brugnera, B. Naroska, private communication.
- [19] M. Cacciari and M. Greco, Phys. Rev. Lett. 73 (1994) 1586; E. Braaten, M.A. Doncheski, S. Fleming and M.L. Mangano, Phys. Lett. 333B (1994) 548; D.P. Roy and K. Sridhar, Phys. Lett. 339B (1994) 141.
- [20] R. Barate et al. [NA-14 Collaboration], Z. Phys. C33 (1987) 505.
- [21] B.H. Denby et al. [FTPS Collaboration], Phys. Rev. Lett. 52 (1984) 795.
- [22] J.J. Aubert et al. [EMC Collaboration], Nucl. Phys. B213 (1983) 1, Z. Phys. C56 (1992) 21.
- [23] D. Allasia et al. [NMC Collaboration], Phys. Lett. 258B (1991) 493.
- [24] S.J. Brodsky, W.K. Tang and P. Hoyer, SLAC-PUB-95-6858.



- [25] H. Jung, D. Krücker, C. Greub and D. Wyler, *Z. Phys.* C60 (1993) 721.
- [26] W.Y. Keung and I.J. Muzinich, *Phys. Rev.* D27 (1983) 1518.
- [27] M. Krämer, Ph. D. Thesis, Univ. Mainz, 1994; J. Zunft, Ph. D. Thesis, Univ. Hamburg, 1994.
- [28] M. Krämer, J. Zunft, J. Steegborn and P.M. Zerwas, *Phys. Lett.* 348B (1995) 657.
- [29] M. Krämer, DESY-95-046, to appear in the Proceedings “Heavy Quark Physics”, Bad Honnef, Germany, 1994.
- [30] L.D. Landau, *Dokl. Akad. Nauk USSR* 60 (1948) 207; C.N. Yang, *Phys. Rev.* 77 (1950) 242.
- [31] B. Guberina, J.H. Kühn, R.D. Peccei and R. Rückl, *Nucl. Phys.* B174 (1980) 317.
- [32] R.K. Ellis and P. Nason, *Nucl. Phys.* B312 (1989) 551.
- [33] J. Smith and W.L. van Neerven, *Nucl. Phys.* B374 (1992) 36.
- [34] J. Collins, F. Wilczek and A. Zee, *Phys. Rev.* D18 (1978) 242; W.J. Marciano, *Phys. Rev.* D29 (1984) 580.
- [35] W. Beenakker, H. Kuijff, W. van Neerven and J. Smith, *Phys. Rev.* D40 (1989) 54.
- [36] G. Passarino and M. Veltman, *Nucl. Phys.* B160 (1979) 151.
- [37] P. Nason, S. Dawson and R.K. Ellis, *Nucl. Phys.* B303 (1988) 607.
- [38] W.A. Bardeen, A.J. Buras, D.W. Duke and T. Muta, *Phys. Rev.* D18 (1978) 3998.
- [39] A. Sommerfeld, *Atombau und Spektrallinien*, Vieweg 1939.
- [40] I. Harris and L.M. Brown, *Phys. Rev.* 105 (1957) 1656.
- [41] J. Kubar André and F.E. Paige, *Phys. Rev.* D19 (1978) 221; B. Humpert and W.L. van Neerven, *Nucl. Phys.* B184 (1981) 225.
- [42] E. Laenen, S. Riemersma, J. Smith and W.L. van Neerven, *Nucl. Phys.* B392 (1993) 162.
- [43] E.G. Floratos, D.A. Ross and C.T. Sachrajda, *Nucl. Phys.* B129 (1977) 66 [Erratum: B139 (1978) 545]; *Nucl. Phys.* B152 (1979) 493; A. Gonzalez-Arroyo, C. Lopez and F.J. Yndurain, *Nucl. Phys.* B153 (1979) 161; A. Gonzalez-Arroyo and C. Lopez, *Nucl. Phys.* B166 (1980) 929; E.G. Floratos, P. Lacaze and C. Kounnas, *Phys. Lett.* 98B (1981) 89, *Phys. Lett.* 98B (1981) 285; W.A. Bardeen and A.J. Buras, *Phys. Rev.* D20 (1979) 166.
- [44] G. Altarelli and G. Parisi, *Nucl. Phys.* B126 (1977) 298.
- [45] M. Glück, E. Reya and A. Vogt, *Z. Phys.* C67 (1995) 433.
- [46] Particle Data Group, *Phys. Rev.* D50 (1994) 1173.
- [47] A. Vogt, *Phys. Lett.* 354B (1995) 145.
- [48] R. Barbieri, R. Gatto and E. Remiddi, *Phys. Lett.* 106B (1981) 497.
- [49] P.M. Stevenson, *Phys. Rev.* D23 (1981) 2916.

- [50] S. Frixione, M.L. Mangano, P. Nason and G. Ridolfi, Nucl. Phys. B431 (1994) 453, Phys. Lett. 348B (1995) 633; M. Drees, M. Krämer, J. Zunft and P.M. Zerwas, Phys. Lett. 306B (1993) 371.
- [51] W. Buchmüller and S.-H.H. Tye, Phys. Rev. D24 (1981) 132.
- [52] S.J. Brodsky, G.P. Lepage and P.B. Mackenzie, Phys. Rev. D28 (1983) 228.
- [53] S. Aid et al. [H1 Collaboration], contribution to the Int. Europhysics Conf. on High Energy Physics, Brussels, 1995.
- [54] M. Derrick et al. [ZEUS Collaboration], contribution to the Int. Europhysics Conf. on High Energy Physics, Brussels, 1995.
- [55] M. Derrick et al. [ZEUS Collaboration], Phys. Lett. 345B (1995) 576; S. Aid et al. [H1 Collaboration], Phys. Lett. 354B (1995) 494.
- [56] A.D. Martin, G. Roberts and W.J. Stirling, Phys. Lett. 354B (1995) 155.
- [57] H.L. Lai, J. Botts, J. Huston, J.G. Morfin, J.F. Owens, J.W. Qiu, W.K. Tung and H. Weerts, Phys. Rev. D51 (1995) 4763.
- [58] A.D. Martin, R.G. Roberts and W.J. Stirling, Phys. Lett. 306B (1993) 145.
- [59] M. Jezabek, J.H. Kühn, Phys. Lett. 316B (1993) 360.